T_2 Accuracy on a Whole-body Imager

by

Warren Donald Foltz

A thesis submitted in conformity with the requirements
for the degree of Masters of Science
Graduate department of Medical Biophysics
University of Toronto

T_2 Accuracy on a Whole-body Imager

Warren Donald Foltz

Masters of Science, 1997

Department of Medical Biophysics

University of Toronto

MR oximetry requires a T_2 measurement technique insensitive to the constraints imposed by a whole-body imager. Simple methods are susceptible to signal loss and tend to underestimate T_2. Current methods use RF pulses or RF cycling patterns which prevent signal loss, yet T_2 tends to be overestimated due to temporary storage of the magnetization along the longitudinal axis, where it decays more slowly with a time constant $T_1 > T_2$. To reduce the T_1 dependence while preventing signal loss, we utilize simple $90_x180_y90_x$ composite pulses and good RF cycling patterns. These methods are critical for T_2 accuracy over a broad range of RF and static field inhomogeneities and refocussing intervals. T_1 signal decay during each $90_x180_y90_x$ pulse must be accounted for to yield T_2 accuracy within 5% when the pulse width is greater than 10% of the refocussing interval. A simple correction scheme compensates for this bias effectively.

Acknowledgements

I would like to thank my supervisor, Dr. Graham Wright. His patience and support have been endless.

I would like to thank my supervisory committee, Dr. Don Plewes and Dr. Peter Burns, for their constructive advice and criticism.

I would like to thank my friends for all the activities which removed me temporarily from the front of a computer screen. In particular, I would like to thank those associated with names such as Hammered Penguins, Pangaea, and Flamengo. I am grateful to you all.

Most of all, I would like to thank Lex and my parents for their continued support.

Contents

List of Tables

List of Figures

Chapter 1

Introduction

1.1 Overview

The capability of magnetic resonance imaging (MRI) to provide excellent soft tissue contrast arises in large part from the dependence of the MR signal on a large number of biophysical parameters. One such parameter is T_2, the time constant which characterises the MR signal decay.

Due to significant variations in T_2 between and within healthy and pathologic tissues, T_2-weighted contrast is used to delineate anatomy and to diagnose pathology. In addition to this qualitative role, previous authors have demonstrated that quantitative measurements of T_2 have potential for assessing function and monitoring disease progression [1, 2].

Our particular interest in T_2 quantitation stems from studies which have demonstrated a strong dependence of blood T_2 on blood oxygen saturation, the percentage of hemoglobin which is oxygenated ($\%O_2$) [3, 4]. Based on this dependence, we are developing MR oximetry, a non-invasive measurement of blood oxygen content using magnetic resonance imaging, into a clinically useful tool.

Unfortunately, typical T_2 measurement techniques are unreliable; they are sensitive

to the hardware limitations associated with a whole-body imager and to the characteristics of the in-vivo environment. This thesis will address these limitations and will present a T_2 measurement technique sufficiently robust for applications on a whole-body imager.

In Chapter 1, I first outline the significance of such a measurement with reference to a specific clinical application, the evaluation of congenital heart defects with shunts. With this as a motivation, I will provide some background on basic MR physics, in particular, T_2 decay and the T_2 measurement technique. Factors which affect T_2 accuracy will be identified and current measurement techniques designed to address these constraints will be reviewed briefly.

In Chapter 2, I design and compare several T_2 measurement techniques and demonstrate their efficacy over the sources of measurement bias identified in Chapter 1. The focus of the development is differential T_1 and T_2 signal decay as magnetization spends time out of the transverse plane. This work includes the design and implementation of a practical correction for T_1 signal decay during composite refocussing pulses. Through the use of refocussing trains composed of simple yet robust composite pulses which allow fast and efficient refocussing, good RF cycling patterns which prevent signal loss at each data acquisition, and our correction scheme, T_2 accuracy within 5% is achieved over conditions typical of a whole-body imager. This chapter has been recommended for acceptance with revisions by the journal "Magnetic Resonance in Medicine" as a full paper.

In Chapter 3, I discuss the original contributions of this work to T_2 quantitation and I introduce future directions. These developments are aimed at further optimization of the *in vivo* T_2 measurement, in particular for MR oximetry. Some preliminary results which explore the effects of flow on T_2 accuracy are presented as a feasibility check.

1.2 Motivation

1.2.1 Oximetry

The determination of vascular oxygen content is of considerable clinical importance as a means to stage and monitor a broad range of conditions [5]. The assessment of shunts in congenital heart disease is the dominant current clinical procedure using knowledge of $\%O_2$ in deep vessels, with roughly 20,000 associated catheterization procedures performed each year in the United States.

1.2.2 Congenital heart disease with shunts

Congenital defects with shunts are present in roughly 0.5% of all live births [6]. The most common shunts occur through either a hole in the septal wall separating the right and left cardiac chambers or between the aorta and pulmonary artery through a patent ductus arteriosus (Fig. 1.1). Blood is usually shunted from the left, or high pressure side of the heart to the right, or low pressure side of the heart, hence, increasing the total pulmonary flow.

Depending on shunt location, these defects can introduce a broad range of hemodynamic conditions. Atrial septal defects are asymptomatic allowing 1.5-4 fold increases in total pulmonary flow with near normal cardiac pressures and minimal increases in flow velocity. Ventricular septal defects increase flow volumes more modestly yet are associated with markedly elevated cardiac pressures and high velocity jets (4 - 5 m/s).

Management of these complex conditions requires the determination of the shunt fraction (SF). SF is the relative volumes of blood flowing through the pulmonary artery and the aorta each minute, such that

$$SF = \frac{Q_p}{Q_s} \tag{1.1}$$

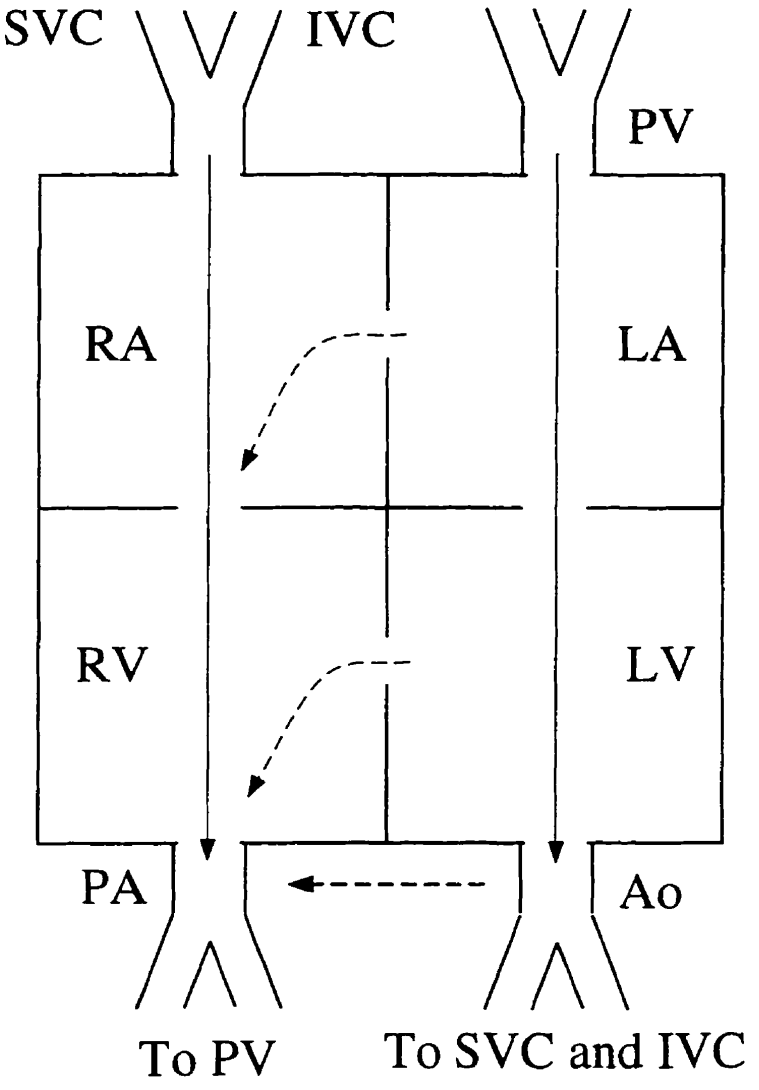

Figure 1.1: Schematic of blood flow through the heart and the surrounding great vessels. The solid arrow depicts the passage of blood under normal conditions. Ideally, blood returning to the heart via the superior and inferior vena cava (SVC and IVC) passes through the right atrium (RA) and enters the right ventricle (RV). Right ventricular contraction forces blood through the pulmonary artery (PA) and into the lungs. This blood returns to the heart via the pulmonary vein (PV) and empties into the left atrium (LA). Left atrial and left ventricular (LV) contraction forces blood out through the aorta (Ao) into the systemic circulation. The locations of the dominant shunts are depicted by the dashed arrows. Blood shunted from left to right bypasses the systemic circulation and re-enters the pulmonary circulation.

where Q_p is the pulmonary blood flow rate and Q_s is the aortic blood flow rate.

Normally, Q_p and Q_s are equivalent and SF $\sim$ 1. SF $>$ 1 signifies increased pulmonary flow. Small shunts (SF between 1 and 1.5) may close spontaneously and tend to be monitored but left untreated. If the shunt is large enough (SF $>$ 1.5), it may cause irreparable damage to the heart and lungs if not surgically treated.

Presently, flow-sensitive Doppler ultrasound and MRI techniques measure cardiac output and shunt fractions with some success within simple shunts [7]. However, the complex geometry associated with many common shunts limits flow accuracy using conventional techniques. Errors associated with quantitative Doppler flow measurements have been well-described [8]. Complex flow patterns in the presence of high velocity jets can present further difficulties.

Oximetric evaluation of shunt fraction

With the significant difficulties encountered by flow-based imaging techniques, the determination of shunt fraction relies on the measures of the changes in blood oxygen saturation which accompany shunt flow. Figure 1.2(a) shows oxygen saturations in and around the heart under normal conditions. Figure 1.2(b) shows oxygen saturations in and around the heart in the presence of a large atrial septal defect (SF $\sim$ 3.3). Thus, for a left to right shunt, blood oxygen saturation within the receiving chamber or vessel increases in proportion to shunt severity.

Currently, measurements of blood oxygen saturation require catheter-based blood draws to access the deep vascular region. Samples are drawn from multiple sites around the right heart during diastole while the patient is at rest [9]. Oxygen saturations are extracted based on differential optical reflectance and transmittance by oxy- and deoxyhemoglobin [10].

A typical 'oximetry run' includes direct sampling of blood within the pulmonary artery (PA), the superior and inferior vena cava (SVC and IVC), the right atrium (RA), and the

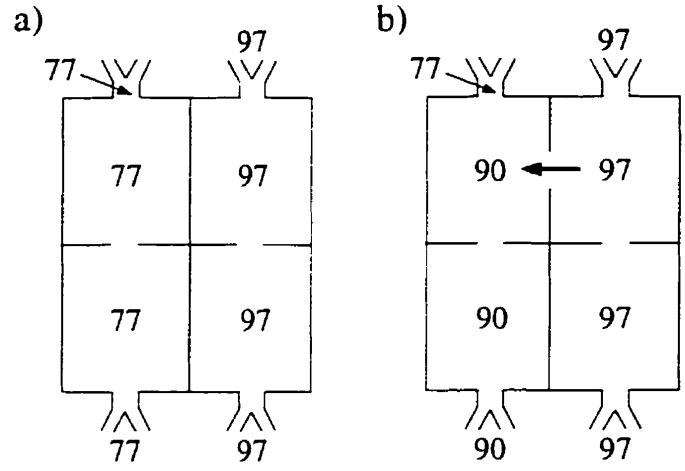

Figure 1.2: Comparison of typical blood oxygen saturations within the deep vasculature (a) under normal conditions; and (b) in the presence of a large atrial septal defect (SF $\sim$ 3.3). Oxygen saturations are increased within the receiving chamber of a left to right shunt.

right ventricle (RV) (Fig. 1.1). Of these, saturations in the SVC and the PA provide the most crucial pieces of information. An increase in oxygen saturation between the SVC and the PA from normal values is indicative of any of the dominant shunts. Sampling in the IVC improves measurement accuracy. Sampling in the RA and the RV helps to localize the position of the defect.

For confident shunt detection, an increase in blood oxygen saturation must be significant relative to the normal variability of such measurements *in vivo*. A large scale study has established the standard deviation of physiological variations to be about $3\%O_2$ [11]. In clinical practice, a $\%O_2$ difference between the SVC and the PA of more than $7\%O_2$, or a difference between the mixed venous contribution ($\%O2_{MV} = 0.7O2_{SVC} + 0.3O2_{IVC}$) and the PA of more than $5\%O_2$, indicates significant shunting (SF $>$ 1.5) [9]. The mixed venous weighting accounts for differential blood flow within the deep veins and for blood flow within the unsampled coronary sinus.

Despite the extreme usefulness of the acquired information, cardiac catheterization is associated with risk and significant morbidity [12]. A non-invasive oximetric evaluation

would reduce the need for catheterization and significantly impact the management of these patients.

Potential non-invasive oximetry methods

Clinical interest in non-invasive oximetry methods has spurred significant developments over the past decade. Near-infrared [13] and time-of-flight [10] spectrophotometry allow estimations of blood oxygen saturation within the deep vascular region. However, complicated scattering behavour of light within heterogeneous tissue renders optical measurements qualitative.

Nuclear magnetic resonance (NMR) and electron paramagnetic resonance (EPR) methods measure the partial pressure of oxygen (pO_2). NMR techniques take advantage of ^{19}F relaxation behaviour in perfluorocarbons [14, 15] and the resonance in the proton spectrum associated with deoxymyoglobin [16]. EPR techniques focus on the linewidth of India ink [17]. For several reasons, these techniques are unlikely to be practical for measurements of vascular $\%O_2$: the relationship between pO_2 and $\%O_2$ is highly non-linear; furthermore, India ink is toxic.

Most MRI methods are based on the differential interaction of diamagnetic oxyhemoglobin and paramagnetic deoxyhemoglobin with an applied magnetic field [3]. Current research includes our own measures of blood T_2 (Fig. 1.3), as well as recent studies which utilize gradient echo methods to measure blood T_2^* [18] or the magnetic field shift within the vessel [19]. These recent techniques allow for more rapid image acquisition, yet they should prove more sensitive to the characteristics of the *in-vivo* environment.

To be clinically useful, MR oximetry must show accuracy at the level of the physiologic noise. Over the clinical range of interest, from 60 to $90\%O_2$, the measured oxygen saturations have a standard deviation of $3\%O_2$. To achieve an oximetry error of $3\%O_2$, we require a T_2 error of 5% [21]. In this work, I optimize the T_2 measurement for 5% accuracy within static

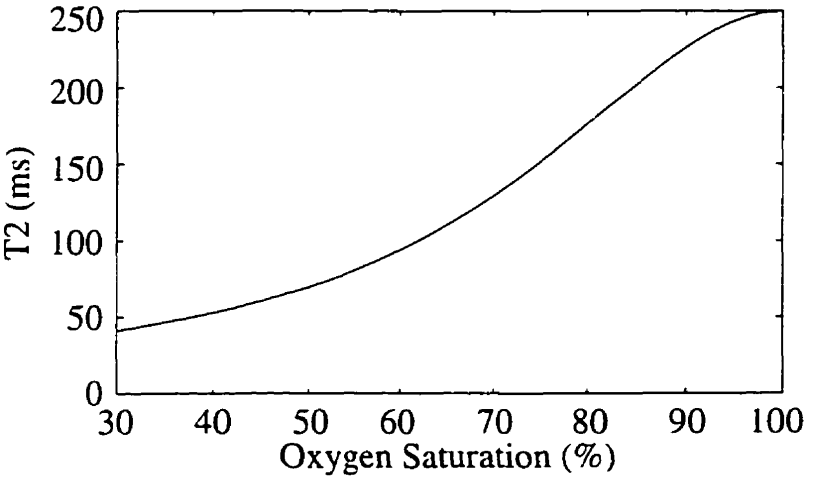

Figure 1.3: Typical dependence of blood T_2 on blood oxygen saturation calculated using simulated data. Note that, based on population data, there is significant individual variation in the T_2-$\%O_2$ relationship. To account for such variation within an MR oximetry study, the T_2-$\%O_2$ relationship must be calibrated for each individual [20].

volumes on a MR imager.

1.3 Basic MR Physics

MR oximetry relies on the nuclear magnetic resonance signal which arises from water protons in the blood. In this section, I describe basic proton magnetic resonance phenomena, in particular T_2^* and T_2 decay and the T_2 measurement technique.

1.3.1 Interaction with a static magnetic field

Many protons are present within the measurement volume. Each proton has an associated dipole moment, enabling it to interact with a magnetic field. When a static magnetic field $\mathbf{B_0}$ is applied, each proton experiences a weak tendency to align parallel to the magnetic field. Such polarization results in a macroscopic magnetization. At thermal equilibrium, this magnetization is aligned along $\mathbf{B_0}$ with magnitude M_o.

Besides its tendency to align, a dipole moment precesses about a magnetic field with

which it is out of alignment. For magnetization out of alignment with $\mathbf{B_0}$, the rate of precession is

$$\omega_o = \gamma B_0 \tag{1.2}$$

where the gyromagnetic ratio, γ, is the proportionality constant. At typical field strengths ($B_0 = 1.5$ Tesla), $f_o = \frac{\omega_o}{2\pi}$ is 63.9 MHz for the proton.

With this behaviour in mind, magnetization can be represented as a 3-D vector, $\mathbf{M}=M_x\mathbf{x}+M_y\mathbf{y}+M_z\mathbf{z}$, where z is the direction of $\mathbf{B_0}$ (Fig. 1.4). For brevity, I describe the component of $\mathbf{M}$ perpendicular to $\mathbf{B_0}$ as a phasor, $M_{xy} = M_x + iM_y$ ($i = \sqrt{-1}$), which precesses about $\mathbf{B_0}$ at a rate, ω_o. The magnitude of the M_{xy} component, $|M_{xy}|$, is the measured MR signal. Only the M_{xy} component decays with a time constant T_2. The M_z component grows towards its equilibrium value with a time constant $T_1 \geq T_2$.

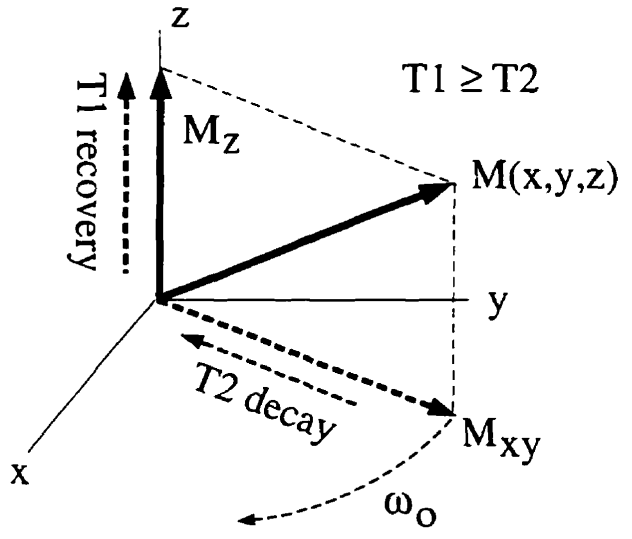

Figure 1.4: 3-D vector model of magnetization and T_1 and T_2 relaxation behaviour. Magnetization equilibrates along the z axis with a time constant T_1. Transverse magnetization precesses about B_0 at a rate ω_o. The measured signal, $|M_{xy}|$, decays with a time constant T_2.

1.3.2 T_2 measurement

For T_2 to be measured, the magnetization initially at equilibrium along the z axis must be rotated to the xy plane. Such manipulation is achieved by applying a magnetic field $\mathbf{B_1}$, which is oscillating at ω_o in resonance with the dipole moments (a radiofrequency or RF wave), in a direction orthogonal to $\mathbf{B_0}$. The effect of such a wave can be visualized within a frame of reference rotating about the z axis at a frequency ω_o (Fig. 1.5). In this reference frame (with axes $x'y'z$), $\mathbf{M}$ will precess about $\mathbf{B_1}$ with a frequency $\omega_1=\gamma B_1$. Precession about $\mathbf{B_1}$ will rotate $\mathbf{M}$ from the z axis and into the $x'y'$ plane.

Typically, $\mathbf{B_1}$ is turned on at a constant RF amplitude for a given duration τ. The resulting $\mathbf{B_1}$ waveform is called a rectangular pulse. Rectangular pulses are characterized based on the rotation angle and axis of rotation of the magnetization. For example, a 90_x excitation pulse will rotate $\mathbf{M}$ about the x' axis to the y' axis (Fig. 1.5).

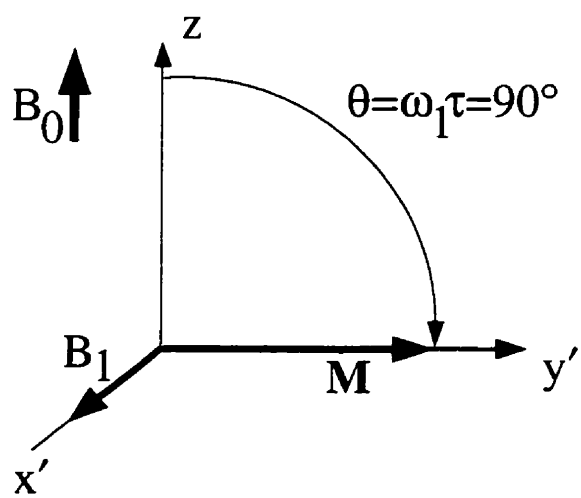

Figure 1.5: In a reference frame rotating around $\mathbf{B_0}$ at the resonance frequency (with axes $x'y'z$), on-resonance magnetization precesses about an applied radiofrequency field of field strength B_1. In this case, B_1 is turned on about the x' axis and rotates $\mathbf{M}$ from the z axis to the y' axis.

T2* decay

Following excitation, the expected T_2 signal decay is not observed. Instead, the signal disappears more rapidly. The resulting signal decay is often characterized as an exponential with a time constant $T_2^* < T_2$.

The mechanics of T_2^* decay are illustrated in Fig. 1.6. Recall that transverse components of **M** precess at a rate proportional to the local field strength (Eq. 1.1). Due to spatial variations in static field strength, components precess at different rates across the measurement volume. In time, components gradually spread out or dephase. Contributions cancel due to destructive interference, leading to loss additional to T_2 decay.

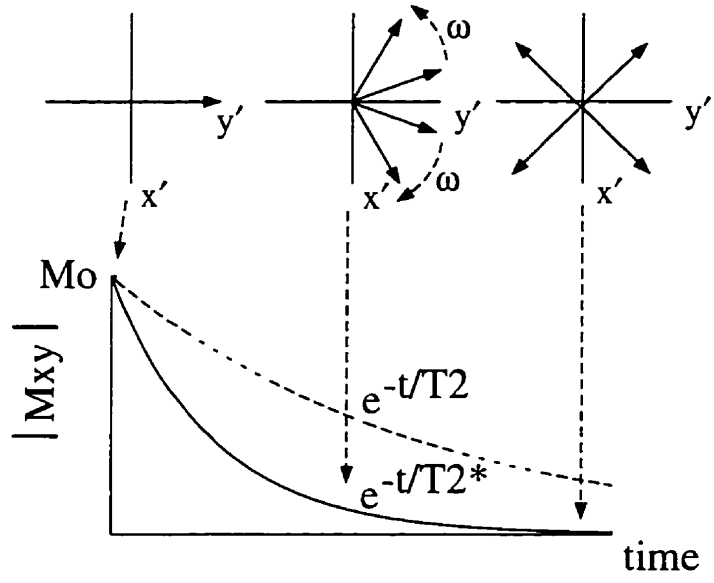

Figure 1.6: Mechanics of T_2^* signal decay. The dashed line depicts the actual T_2 decay curve. The solid line depicts the observed T_2^* decay. Following excitation, all components of **M** are in phase and the signal is a maximum. With time, components of **M** which precess at different rates gradually spread out, losing phase coherence. The measured signal decreases since the individual components do not add constructively.

T_2 measurement technique

To measure T_2, T_2^* decay must be avoided. This is done using a refocussing train. A 90° excitation pulse is followed by a train of 180° rectangular pulses separated by a refocussing interval τ_{180}. Figure 1.7(a) illustrates the mechanics of the first 90_x-180_y segment. Figure 1.7(b) illustrates the change in signal magnitude through the refocussing train. The 90° pulse rotates longitudinal magnetization to the y' axis and the signal is a maximum. Once in the $x'y'$ plane, components evolve for a period $\tau = \tau_{180}/2$ and dephase. This results in signal loss with a time constant T_2^*. Application of a 180_y^o pulse flips these components about the y' axis and reverses the sense of the phase. Assuming the precessional frequencies are constant in time, evolution during an additional period τ leads to a rephasing of the dipole moments along y' at the echo time, TE $= 2\tau$. To measure T_2, the MR signal, $|M_{xy}|$, is measured at each echo time (TE). The resulting curve is fitted, often as a monoexponential decay.

1.4 Factors affecting T_2 accuracy

In principle, the refocussing train provides a convenient means to measure T_2. Regular application of refocussing pulses allows for multiple data acquisitions per excitation [22]. For MR oximetry, it ensures monoexponential signal decay for deoxygenated blood [4].

However, imager-based T_2 quantitation has not generally been successful [23, 24]. Accuracy within the refocussing train is limited by RF amplifier constraints and errors in RF and static field amplitude through the effects of imperfect pulses. The resulting errors have been well described by previous authors [25–28]. In this section, I review the sources of measurement bias which result in imperfect pulses and the effects of such pulses on T_2 accuracy within the refocussing train. To finish, I list typical constraints to which an *in vivo* T_2 measurement technique must be insensitive.

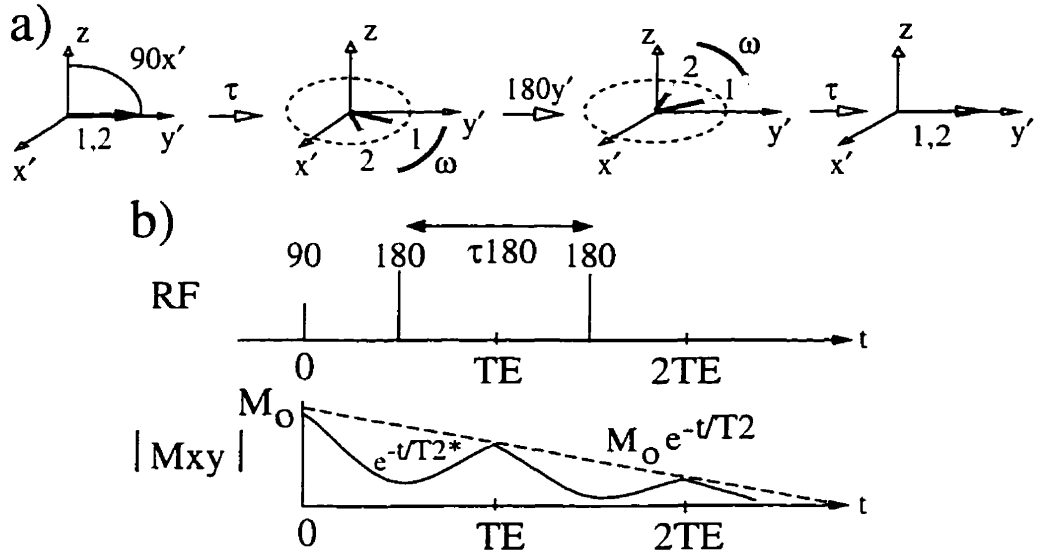

Figure 1.7: T_2 measurement technique. (a) Mechanics of a refocussing pulse. Following excitation, each individual component of the transverse magnetization will precess and accumulate a phase proportional to its local field strength. Following phase reversal by a 180° refocussing pulse applied about the y' axis, these components rephase at the echo time if the local fields are static. (b) Change in signal magnitude through the refocussing train. Application of a train of refocussing pulses allows sampling of signal magnitude at a number of echo times (TE). The resulting envelope is often described by an exponential with time constant T_2.

1.4.1 Sources of measurement bias

The effect of errors in static field amplitude (ΔB_0) can be visualized within the rotating reference frame. Within this frame of reference, off-resonance magnetization is influenced by a longitudinal magnetic field, $\mathbf{\Delta B_0}$, in addition to $\mathbf{B_1}$. Instead of precessing about $\mathbf{B_1}$, magnetization will precess about the net magnetic field, $\mathbf{B_{eff}}$, which has magnitude $\sqrt{B_1^2 + \Delta B_0^2}$ and is offset from the transverse plane by an angle $\phi = \text{atan}(\Delta B_0/B_1)$ (Fig. 1.8(a)).

With errors in RF amplitude (ΔB_1), the angle of rotation will not be ideal. Assuming $B_{eff} \sim B_1$ so that $\theta \sim \gamma B_1 \tau$, an error in RF amplitude will lead to an error in rotation angle $\Delta\theta \sim \gamma \Delta B_1 \tau$ (Fig. 1.8(b)). The error in rotation angle is a minimum when $\mathbf{M}$ is aligned with $\mathbf{B_1}$ at the time of refocussing and no rotation occurs ($\gamma \Delta B_0 \tau_{180}/2 = 0$). The error is a

maximum when $\mathbf{B_1}$ is orthogonal to $\mathbf{M}$ at the time of refocussing ($\gamma\Delta B_0\tau_{180}/2 = \pi/2$) and the arc length of rotation is the greatest.

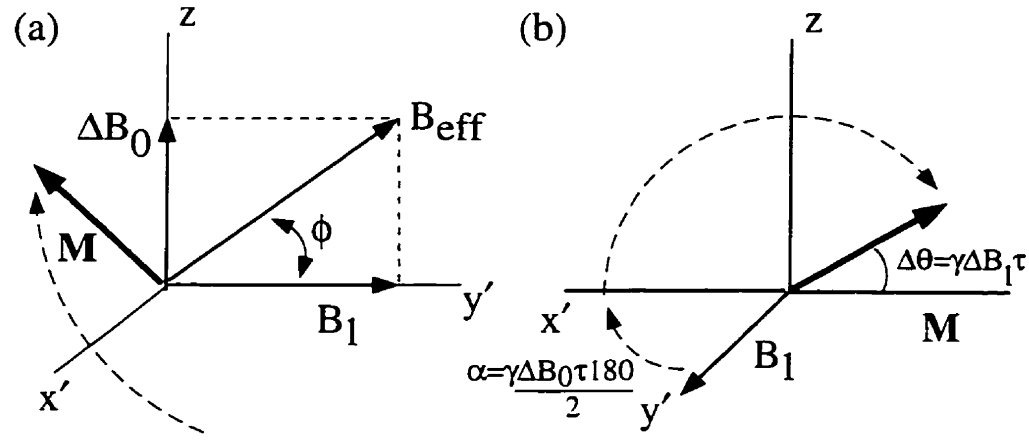

Figure 1.8: Criteria for good refocussing using rectangular pulses. (a) Within the rotating frame, off-resonance magnetization ($\mathbf{M}$) precesses about an effective field B_{eff} oriented outside of the $x'y'$ plane. Sufficiently high RF amplitudes ($B_1 >> \Delta B_0$) are required for $\mathbf{M}$ to precess about $\mathbf{B_1}$. (b) Errors in RF amplitude result in nonideal rotation angles. Assuming rotations about $\mathbf{B_1}$, $\Delta\theta = \gamma\Delta B_1\tau$, this error is maximized when $\alpha = \gamma\Delta B_0\tau_{180}/2 = \pi/2$. A rotation angle of 180^o is required to return off-resonance $\mathbf{M}$ to the $x'y'$ plane.

An ideal rectangular refocussing pulse will rotate off-resonance magnetization by 180^o about $\mathbf{B_1}$ to return it to the xy plane. To do this, the effects of ΔB_0 and ΔB_1 must be minimized. This requires RF amplitudes which are sufficiently high ($B_1 >> \Delta B_0$) such that $\phi \sim 0$ (Fig. 1.8(a)), and sufficiently accurate such that $\theta = \gamma B_1\tau = \pi$ (Fig. 1.8(b)).

However, these conditions are not well satisfied on a whole-body imager. With inherent constraints to RF amplitude using the body coil to transmit, B_1 is often on the order of $10\Delta B_0$; thus, $\phi \neq 0$. As well, variations in RF field strength across the measurement volume lead to spatially-dependent rotation angles; thus, $\theta \neq \pi$. Hence, for *in vivo* measurements, both the axis and the angle of rotation will not be ideal. A single imperfect refocussing pulse will leave $\mathbf{M}$ outside the xy plane, producing three components: 1) a transverse component which refocusses at the echo time; 2) a transverse component which does not refocus at the

echo time; and 3) a longitudinal component [29]. Neither of the latter two components will be measured and the MR signal will be reduced.

1.4.2 Effects of imperfect pulses

Within a refocussing train, imperfect refocussing pulses can lead to systematic error in T_2 through four mechanisms:

1. Magnetization can be rotated to the z axis where it will not be measured.

2. Transverse magnetization which does not refocus will not be measured.

3. Magnetization rotated to the z axis can be returned to the xy plane following subsequent imperfect pulses. The decay of magnetization stored temporarily along the z axis will exhibit a T_1 dependence.

4. Imperfections in the excitation pulse will leave a component of $\mathbf{M}$ along the z axis. Magnetization left along the z axis following a poor excitation can be rotated to the xy plane by 'refocussing pulses' where it will be included in the measurement.

The first two errors lead to signal loss. If these effects are cumulative, T_2 will be underestimated. The final two errors enhance signal magnitude. If these effects are cumulative, T_2 will be overestimated (Fig. 1.9).

1.4.3 Constraints on T_2 accuracy

To account for these effects *in vivo*, the T_2 measurement must be insensitive over the following constraints:

1. Differences in magnetic susceptibility within the body can lead to static field variations (ΔB_0) occasionally as large as ± 10 parts per million (ppm) across an imaging slice.

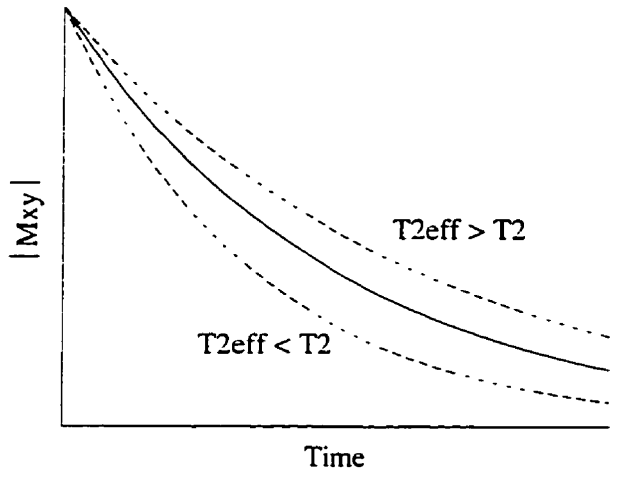

Figure 1.9: Imperfect pulses degrade T_2 accuracy. The solid line depicts the correct signal decay curve. The dashed lines depict erroneous measurements. If effects which cause signal loss are dominant, magnetization will appear to be decaying more rapidly and the T_2 estimate will be low ($T_{2,eff} < T_2$). If effects which cause signal enhancement are dominant, signal will appear to decay less rapidly and the T_2 estimate will be high ($T_{2,eff} > T_2$)

However, the susceptibilities of most soft tissues are estimated to be well within ± 2 ppm [30]. On a typical whole-body imager ($B_0 = 1.5$ Tesla), 2 ppm corresponds to 128 Hz.

2. RF amplifiers cannot transmit at amplitudes greater than 0.23 Gauss using the body coil. An RF amplitude of 0.23 Gauss corresponds to a precessional frequency of 1 kHz within the rotating frame (Sec. 1.3.2). Typical RF amplitudes are lower ($\frac{\gamma}{2\pi}B_1$ from 600 to 800 Hz) to avoid excessive heat deposition and to allow for different coil loading in different patients.

3. RF penetration effects and coil imperfections can lead to nonuniform RF intensities (ΔB_1) across an excited volume. These field variations tend to be within 15% [31].

4. At typical static field strengths (≤ 1.5 Tesla), $T_1/T_2 > 4$ in the majority of biological tissues and pathologies [32, 33].

5. The refocussing interval, τ_{180}, is limited by RF amplifier constraints and body heating ($\tau_{180} > 5$ms). Accuracy over a broad range of τ_{180} may be desirable to utilize τ_{180}-dependent contrast [4] and to characterize the complicated signal decay in biological tissue [34].

1.5 T2 measurement techniques

Considerable work has been performed to improve the accuracy of the T_2 measurement. The signal-to-noise ratio can be optimized with proper sampling strategy [35]. Problems associated with image artifacts [34, 36, 37] and measurement reproducibility have been dealt with satisfactorily [38–40]. Eddy currents associated with the readout gradient can be compensated for effectively [41]. Even with these improvements, the effects of imperfect pulses remain significant obstacles to T_2 accuracy on a whole-body imager.

The dominant problem associated with nonideal refocussing has been signal loss at each data acquisition. With imperfect refocussing, a component of **M** can be rotated to the z axis or can remain unrefocussed within the xy plane and hence will be dephased when signal is measured.

This signal loss can be avoided using sequences of rectangular pulses which self-compensate for pulse imperfections. Following each sequence, the cumulative effect of pulse errors tends to zero and refocussing is good. With continual repetition of this pulse sequence through the refocussing train, the magnetization is periodically well-refocussed allowing multiple data acquisitions per excitation.

Such sequences of rectangular pulses form the basis of many current T_2 measurement techniques. They have been implemented into the refocussing train using two approaches:

1. The phases of subsequent refocussing pulses can be manipulated in patterns which self-compensate for ΔB_0 and/or ΔB_1. The most common example is the Carr-Purcell-

Meiboom-Gill RF cycling pattern, or CPMG [42]. This cycling pattern introduces a 90^o phase shift between the excitation pulse (90_x) and the train of refocussing pulses (180_y) to correct for ΔB_1 following every even-numbered pulse. Other RF cycling patterns, namely MLEV [43,44] and XY [45–47], self-compensate for both ΔB_0 and ΔB_1 yet require longer and more complex phase patterns. With longer phase patterns, accurate sampling of the signal decay curve will be less frequent.

2. A self-compensating sequence of rectangular pulses can be incorporated as a single composite refocussing pulse. Many such composite pulses exist [48]. More complex pulses trade off pulse brevity and RF power deposition for increased ΔB_0 and/or ΔB_1 insensitivity.

   The most common example is the three-pulse sequence, $90_x180_y90_x$. This pulse is relatively simple yet it provides good compensation for ΔB_1 with only a two-fold increase in pulse duration [49].

   Several composite pulses provide dual ΔB_0 and ΔB_1 compensation. However, most designs rely on recursive expansions which are not optimal and pulse durations tend to be too long for clinical application. For T_2 quantitation, refocussing pulse design has been numerically optimized by Poon et al [50]. In conjunction with an effective spoiler gradient pattern, the resultant sixteen-pulse sequence, the version S pulse, was demonstrated to provide T_2 quantitation superior to existing techniques [34].

However, even with these corrections, the T_2 measurement may not be accurate. At intermediate stages of each sequence, when refocussing is poor, magnetization is temporarily stored along the longitudinal axis where it decays more slowly with a time constant $T_1 > T_2$. In Chapter 2, I demonstrate that bias from T_1 signal decay may be excessive using current techniques and suggest new methods to address these difficulties.

Chapter 2

T_2 Accuracy on a Whole-body Imager

2.1 Introduction

Current T_2 measurement techniques rely on RF cycling patterns or composite pulses to self-compensate for the effects of imperfect pulses periodically. At the end of each period, magnetization is refocussed well within the xy plane. Synchronization of data acquisition with the end of each period renders the T_2 measurement insensitive to signal loss.

However, a periodic correction is inherently sensitive to measurement bias on a whole-body imager. With degraded refocussing at intermediate stages of each period, magnetization is temporarily stored along the longitudinal axis. As a result, these methods tend to overestimate T_2.

In this chapter, I will show that differential signal decay along the z axis and within the xy plane is a significant source of error within the refocussing train, especially with current methods that minimize signal loss in the presence of RF and static field inhomogeneities. An alternative refocussing train which more fully satisfies the constraints identified in Ch. 1 will be proposed. Through simulation and experiment I will show that this train preserves T_2 accuracy within 5% over a broad range of conditions typical of a whole-body imager.

Finally I will discuss some of the practical issues of this design.

2.2 Theory and Background

2.2.1 T_1 signal decay

In the absence of refocussing pulses, the relaxation behaviour of longitudinal magnetization is often described as an exponential growth with time constant T_1, such that

$$M_z(t) = M_z(t=0)e^{-t/T_1} + M_o(1 - e^{-t/T_1}) \tag{2.1}$$

where M_o is the equilibrium magnetization. The initial magnetization along the z axis, M_z(t=0), decays with a time constant T_1. Meanwhile, an additive T_1-dependent recovery term increases the longitudinal magnetization, $M_o(1 - e^{-t/T_1})$.

Within a refocussing train, only the T_1 decay term contributes to relaxation behaviour along the z axis ($M_z(t) = M_z(t=0)e^{-t/T_1}$). Regular application of refocussing pulses cycles the longitudinal magnetization between the $\pm$z axes. The additive contributions before and after each refocussing pulse have the opposite sign. At each echo time, these contributions have equal magnitude and therefore cancel.

With this in mind, the mechanics of T_2 bias from T_1 signal decay are illustrated in Fig. 2.1. Within a refocussing train, transverse magnetization decays with a time constant T_2 and longitudinal magnetization decays with a time constant T_1. With $T_1 > T_2$, signal stored temporarily along the z axis will decay more slowly resulting in an overestimation of T_2 [25, 26].

To visualize the effects of T_1 signal decay and the other biases within the refocussing train better, a computer model was developed. The simulation cascaded the solution to the Bloch equations from each part of the refocussing train for magnetization at a single resonance frequency using measured relaxation times as input. The solution accounted for

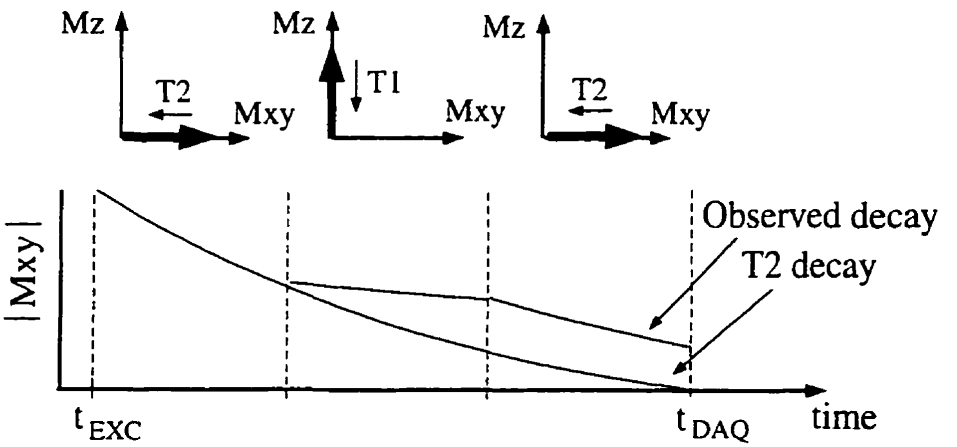

Figure 2.1: Signal decay behaviour within a refocussing train. Following excitation (t=t_{EXC}), regularly refocussed magnetization within the xy plane decays with a time constant T_2. However, any magnetization rotated to the z axis within the refocussing train will decay more slowly with a time constant $T_1 > T_2$. If this magnetization is returned to the xy plane and measured at t=t_{DAQ}, its magnitude will be artificially high resulting in an overestimation of T_2.

pulse type, τ_{180}, phase pattern, the effects of relaxation and errors in RF and static field amplitude between each pulse, the effects of relaxation and errors in RF and static field amplitude during each pulse [51], and phase-cycling. To calculate T_2, the signal magnitude was extracted at the desired echo times and fitted as a monoexponential decay using a least squares fit [35].

Through theory and simulation, I will demonstrate how differential signal decay can introduce excessive measurement error in current T_2 measurement techniques. RF-cycled trains of rectangular pulses are sensitive to T_1 signal decay between each RF pulse. Trains of composite pulses are sensitive to T_1 signal decay during each RF pulse.

2.2.2 T_1 signal decay between rectangular pulses

RF cycling patterns provide good refocussing across multiple imperfect pulses. However, with poorer refocussing at intermediate stages in the cycling pattern, magnetization will

temporarily be stored along the z axis between refocussing pulses. This error is illustrated in Fig. 2.2 using rectangular pulses in the CPMG pattern.

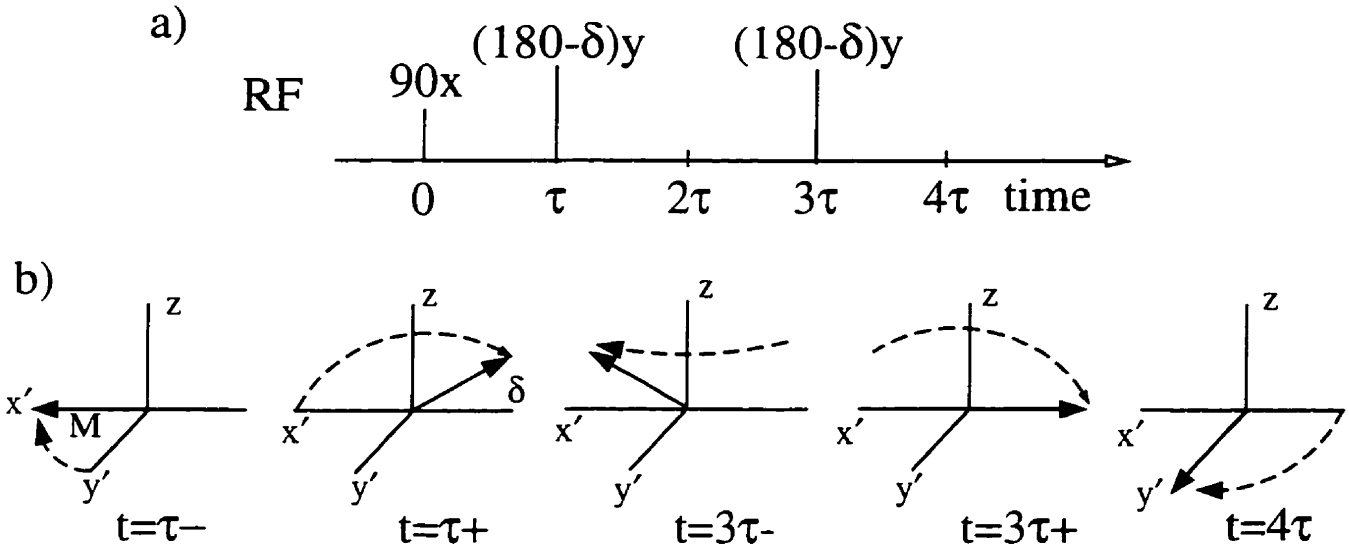

Figure 2.2: Using RF cycling patterns, magnetization spends time along the z axis between imperfect refocussing pulses. (a) CPMG pattern. This pattern introduces a 90° phase shift between the excitation pulse and the train of refocussing pulses. In this case, the refocussing pulses have an error in rotation angle, δ. (b) Mechanics of CPMG pattern. Within the rotating frame, the excitation pulse (90_x) rotates magnetization from the z axis to the y' axis. Following excitation, off-resonance magnetization evolves for a period τ into the $x'y'$ plane. At this time, a rectangular pulse with an error in flip angle, δ, is applied. M is rotated around $\mathbf{B_1}$ (the y' axis) to a point above $x'y'$z plane. Following further evolution for a period 2τ, a second imperfect refocussing pulse returns **M** to the transverse plane correcting for ΔB_1. Evolution for an additional period, τ, realigns **M** along y' at the echo time. Hence, with errors in RF amplitude, magnetization is stored along the longitudinal axis during the refocussing interval from t = τ to t = 3τ.

Following excitation (90_x), the M_y component precesses into the xy plane. Precession is due to phase accumulation in the presence of ΔB_0. With typical errors in RF amplitude, a rectangular pulse (180_y) may rotate a significant portion of magnetization along the x' axis to the z axis temporarily. The M_z component is maximum when **M** is perpendicular to B_1 at the time of refocussing (Fig. 1.6). Following evolution for a period τ_{180}, the longitudinal

component is returned to the xy plane by a second imperfect refocussing pulse. Upon return to the xy plane, the decay of this component may exhibit sufficient T_1 dependence to result in an excessive overestimation of T_2. Specifically (see Fig. 2.3), $\Delta B_1 > 5\%$ introduces a T_2 error $> 5\%$ for typical values of T_1/T_2. No RF cycling pattern can remove this error. Since phase accumulation cannot be avoided on a whole-body imager ($\Delta\phi = \gamma\Delta B_0\tau_{180}/2 = \pi/2$ for $\gamma\Delta B_0 = 25$ Hz and $\tau_{180} = 20$ ms), a better refocussing pulse is essential.

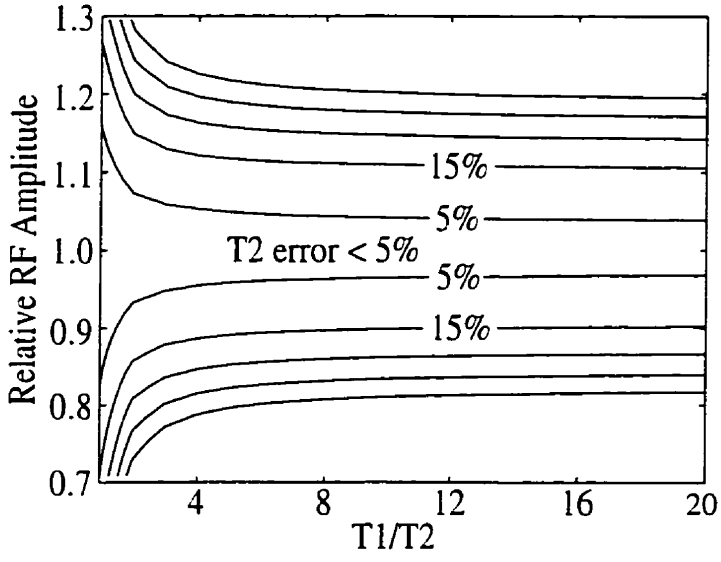

Figure 2.3: Trains of rectangular pulses tend to overestimate the T_2 of off-resonance magnetization. Using simulated data, this contour plot demonstrates that T_2 error will be excessive ($> 5\%$) for$\Delta B_1 > 5\%$ and $T_1/T_2 > 4$ when $\gamma\Delta B_0/(\tau_{180}/2) = \pi/2$. The simulation assumes high RF amplitudes so that errors during the pulse other than ΔB_1 are negligible.

2.2.3 T_1 signal decay during composite pulses

The ability of some composite pulses to refocus the magnetization over a broad range of ΔB_0 and ΔB_1 has been well-documented [48, 49]. As a result, the T_2 measurement is insensitive to T_1 signal decay between each pulse. However, to gain this insensitivity, magnetization spends time along the z axis during each pulse. This error is illustrated in Fig. 2.4 using an ideal $90_x180_y90_x$ pulse.

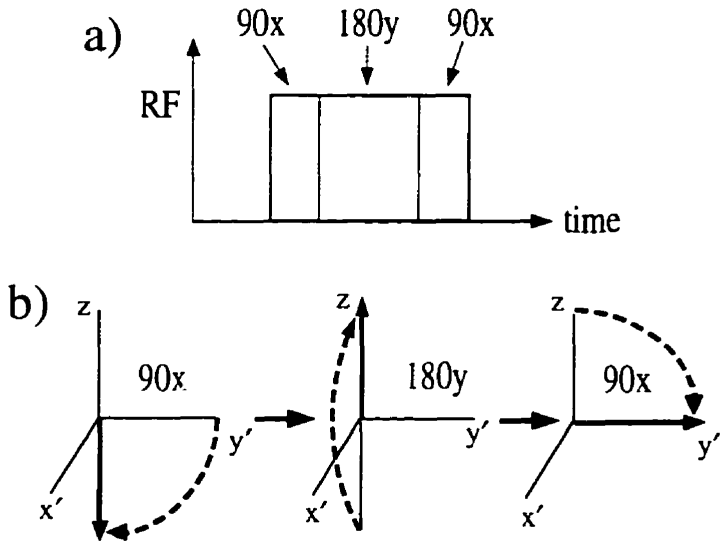

Figure 2.4: Magnetization is rotated to the z axis during a composite pulse. (a) The $90_x180_y90_x$ pulse; and (b) rotation of magnetization during an ideal $90_x180_y90_x$ pulse. Within the rotating frame, magnetization is initially along the y' axis. The 90_x pulse rotates magnetization to the -z axis. The second pulse rotates magnetization by 180° to the z axis. The final pulse returns magnetization to the y' axis.

Characterization of the resulting bias requires an understanding of signal decay during RF pulses. Very high RF amplitudes introduce spin-locking where the components of **M** are 'locked' along $\mathbf{B_1}$ and signal decay times are altered to $T_{1\rho}$ [52]. However, for $\frac{\gamma}{2\pi}B_1 \leq 1$ kHz, signal decay is well-characterized by considering the orientation of **M** at each instant in time, t, during an RF pulse. Over a small time interval centered about t, the M_z component decays with a time constant T_1 and the M_{xy} component decays with a time constant T_2.

Due to the simple trajectory, the effects of differential signal decay during the $90_x180_y90_x$ pulse can be readily quantified (Fig. 2.5). The M_y component is rotated by 2π radians so that T_1 and T_2 decay each occur for a half of every pulse duration (pw). The M_x component is rotated by π radians and decays with a time constant T_1 for a quarter of every pulse duration.

Within a refocussing train, the extent of this error will depend upon the RF cycling pattern of refocussing pulses and the fraction of time spent along the z axis relative to the

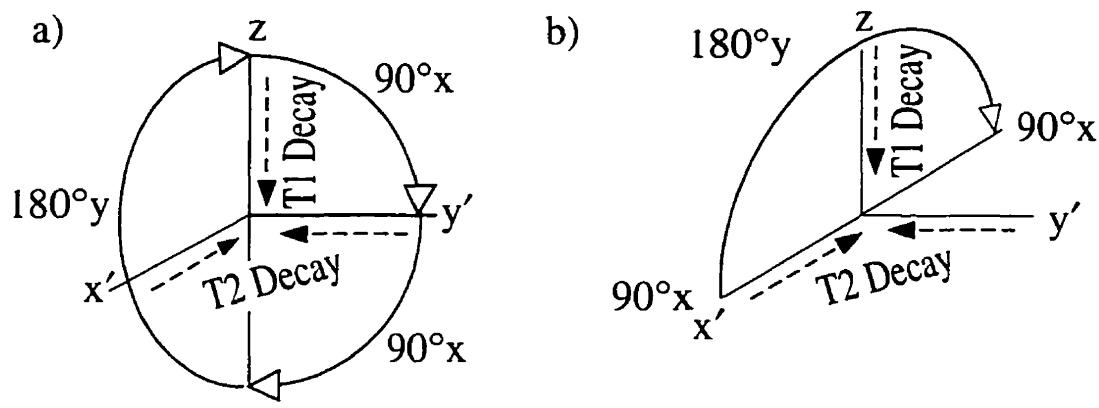

Figure 2.5: Signal decay behaviour during an $90_x180_y90_x$ composite pulse ($\frac{\gamma}{2\pi}B_1 < 1$ kHz) is dependent on the phase of the transverse magnetization. The arrows represent the trajectory of the magnetization within the rotating frame: (a) Decay of the M_y component. By circular symmetry, the M_y component spends equal time along the z axis and within the $x'y'$ plane and decays with time constants T_1 and T_2 for equal periods of time; and (b) Decay of the M_x component. The M_x component is aligned with the rotation axis of each 90_x pulse and remains along the x' axis. Magnetization is rotated to the z axis during the 180_y pulse. Signal decays with a time constant T_1 for a quarter of every pulse and a time constant T_2 for the remaining pulse duration.

refocussing interval (pw/τ_{180}). As indicated in Sec. 1.5, several RF cycling patterns exist with differing sensitivities to ΔB_0 and ΔB_1. We will consider the severity of T_1 signal decay using composite pulses in each of these RF cycling patterns. The phases of the first 16 pulses in CPMG, MLEV, and XY are summarized in Table 2.1. Assuming ideal pulses, CPMG and MLEV continually refocus the M_y component; hence, Fig. 2.5(a) applies. XY cycles subsequent pulses between the ±x and ±y axes; hence, the magnetization is subject to the relaxation behaviour depicted in Fig. 2.5(a) and Fig. 2.5(b) on successive pulses.

As a result of this bias, an echo time (TE) following a refocussing train is composed of a period of T_2 decay and a period of T_1 decay. For an ideal CPMG or MLEV train, there is no signal decay for half of every pulse duration, assuming $T_1 >> T_2$. In this case, the actual period of T_2 decay (TE_{corr}) at an echo time is

$$\mathrm{TE}_{corr} = \mathrm{TE} - k * 0.5 * pw \tag{2.2}$$

RF cycling pattern	Axis of rotation
CPMG	$yyyy\ yyyy\ yyyy\ yyyy$
MLEV	$yy\bar{y}\bar{y}\ \bar{y}yy\bar{y}\ \bar{y}\bar{y}yy\ y\bar{y}\bar{y}y$
XY	$yxyx\ xyxy\ \bar{y}\bar{x}\bar{y}\bar{x}\ \bar{x}\bar{y}\bar{x}\bar{y}$

Table 2.1: Refocussing scheme of CPMG, MLEV, XY RF cycling patterns. The letters represent the axis of rotation of subsequent refocussing pulses within the rotating frame. The bars represent rotations about the corresponding negative axes. Using the $90_0180_{90}90_0$ composite pulses, the above axes refer to the axis of rotation of the 180° pulse. All patterns assume a 90_x excitation.

where $k = \mathrm{TE}/\tau_{180}$ is the number of refocussing pulses up to that echo time, since this is a cumulative effect.

If unaccounted for, this overestimation should lead to an approximate expected error of

$$\frac{\Delta T_2}{T_2} \simeq \frac{\mathrm{TE} - \mathrm{TE}_{corr}}{\mathrm{TE}_{corr}} \simeq \frac{0.5 * pw}{\tau_{180} - 0.5 * pw} \simeq \frac{0.5 * pw}{\tau_{180}}. \tag{2.3}$$

This linear relationship between ΔT_2 and ΔTE is calculated using the difference between the first two terms of a Taylor expansion of an exponential decay at two echo times. This relationship is an approximation which may not prove valid at larger values of pw/τ_{180}. In this regime, differences between higher-order terms in the Taylor expansions may become significant.

Using XY, there is no signal decay for half of one pulse duration and a quarter of the successive pulse duration, assuming $T_1 >> T_2$. Taking the average of these values, signal does not decay during 3/8 of every pulse duration. The actual period of T_2 decay is

$$\mathrm{TE}_{corr} = \mathrm{TE} - k * \frac{3}{8} * pw. \tag{2.4}$$

The corresponding approximate expected error using XY is

$$\frac{\Delta T_2}{T_2} \simeq \frac{\mathrm{TE} - \mathrm{TE}_{corr}}{\mathrm{TE}_{corr}} \simeq \frac{\frac{3}{8} * pw}{\tau_{180} - \frac{3}{8} * pw} \simeq \frac{\frac{3}{8} * pw}{\tau_{180}}. \tag{2.5}$$

With typical RF amplitudes ($\frac{\gamma}{2\pi}B_1 \sim 600$ Hz) and on-resonance magnetization, 5% error in T_2 will result for $\tau_{180} < 18$ ms using CPMG or MLEV and $\tau_{180} < 12.6$ ms using XY

(Fig. 2.6). This is a significant constraint and must be corrected for in a measurement of absolute T_2 values.

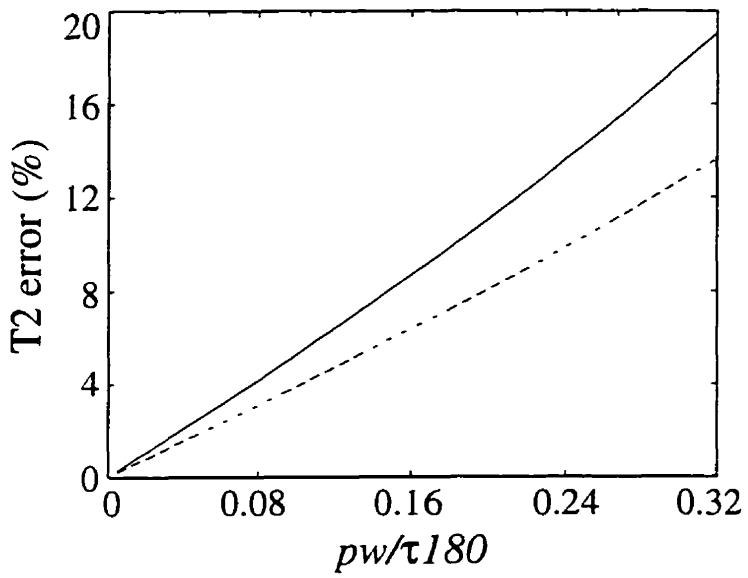

Figure 2.6: As the pw/τ_{180} ratio increases, the period of T_1 signal decay increases resulting in a greater overestimation of T_2. Using simulated data ($T_1 >> T_2$), the contribution of T_1 signal decay to T_2 error is illustrated during (solid line) CPMG and MLEV and (dashed line) XY trains of ideal $90_x180_y90_x$ composite pulses of variable pulse duration. Refocussing interval was held constant. The relationship between T_2 error and pw/τ_{180} clearly deviates from linearity at larger values of pw/τ_{180}.

2.3 Methods

2.3.1 Overview

To account for the effects of differential signal decay during the refocussing train, the design of the T_2 measurement must be guided by the following principles:

1. The refocussing train must include composite pulses.

2. Trains of shorter and hence simpler composite pulses are preferable for several reasons: a) bias from differential signal decay during each pulse is less severe; and b) heat

deposition is decreased for a given τ_{180}.

3. For T_2 accuracy within 5%, some correction for differential signal decay during composite pulses will be necessary when $pw/\tau_{180} > 0.1$.

I will start at the simplest level, the $90_x180_y90_x$ composite pulse. Previous work has demonstrated a single $90_x180_y90_x$ pulse can refocus well (> 95% efficiency) over expected ranges of inhomogeneities at typical RF amplitudes ($\frac{\gamma}{2\pi}B_1 > 600$ Hz) [34]. However, for T_2 accuracy within 5% over a broad range of refocussing intervals, bias from T_1 signal decay during each pulse must be accounted for. A practical correction to compensate for this bias has been designed and implemented. With the combination of good pulses and our correction scheme, the T_2 measurement should be insensitive to bias from differential signal decay.

As stated in the previous chapter, refocussing train design must also minimize errors due to ΔB_1 and ΔB_0 at each data acquisition. In the absence of spoiler gradients, good RF cycling patterns can suffice. Using an experimental and a simulated pulse sequence designed to isolate the role of the refocussing train within a T_2 measurement, I have compared the ability of the CPMG, MLEV, and XY RF cycling patterns to preserve T_2 contrast during trains of $90_x180_y90_x$ composite pulses. With dual ΔB_0 and ΔB_1 compensation, I expect MLEV and XY to provide superior T_2 accuracy to CPMG, especially in longer refocussing trains.

To verify the need for composite pulses and the severity of differential signal decay during these pulses and to demonstrate the performance of the proposed refocussing trains and our correction, a series of three experiments were performed. Before describing these experiments in greater detail, I will provide a description of both our correction scheme and the experimental set-up.

2.3.2 Correction for T_1 signal decay during each composite pulse

For the simple case of ideal pulses and $T_1 >> T_2$, Eqs. [2.2] through [2.5] suggest T_2 can be measured accurately using the corrected echo times (TE_{corr}) in a least-squares fit [35]. Such a TE shift will not be optimal on a whole-body imager due to non-negligible T_1 signal decay and RF and static field inhomogeneities. In this section, I design a TE correction which accounts for T_1 signal decay yet is insensitive to ΔB_0 and ΔB_1. This development is described in detail for CPMG and MLEV and briefly for XY.

To start, Eq. [2.2] must be generalized to account for non-negligible T_1 decay. A simple comparison of the exponents of T_1 and T_2 decay reveals that T_1 decay for half of every pulse duration is equivalent to T_2 decay for the fractional period $T_2/(2T_1)$.

This period of equivalent T_2 decay while magnetization is along M_z shortens the periods in Eq. [2.2] when no decay occurs. The corrected echo times (TE_{corr}) are

$$TE_{corr} = TE - k * (0.5 - \frac{T_2}{2 * T_1}) * pw \tag{2.6}$$

where $k = TE/\tau_{180}$ is the number of refocussing pulses at each echo time. The latter part of Eq. 2.6 represents the period during each echo time when effectively no decay occurs.

In the general case, knowledge of relaxation times may not readily be available and I must assume a value δ for $T_2/(2T_1)$. Over the physiologic range of interest ($T_1/T_2 = 4$ to 10), δ varies slowly, from 0.125 to 0.05. Such insensitivity suggests an optimal value for δ should provide sufficient accuracy over the desired range.

T_2 error is minimized over the physiologic range of T_1/T_2 and a reasonable range of pw/τ_{180} when $\delta \sim 0.088$. Using this optimal value, T_2 error is less than 1.4% for T_1/T_2 greater than 4 and pw/τ_{180} less than 0.32. For the majority of applications, pw/τ_{180} is less than 0.16 and T_2 error will tend to be less than 0.6%.

However, problems will arise with this correction due to static and RF field inhomogeneities which compromise the symmetry of the refocussing pulse. Based on Fig. 2.5,

off-resonance magnetization is less sensitive than on-resonance magnetization to T_1 signal decay during CPMG or MLEV. Hence, the on-resonance correction, $\delta = 0.088$, will underestimate the effective echo times for off-resonance magnetization. Simulations suggest this overcompensation should be excessive only for $\gamma\Delta B_0\ \tau_{180}/2 \sim \pi/2$ and $pw/\tau_{180} \geq 0.2$ (at resonance offsets $\geq$ 1 ppm with $\tau_{180} \leq$ 8ms and $\frac{\gamma}{2\pi}B_1 = 620$ Hz). Errors associated with ΔB_1 tend to be within 2%.

Following a similar development, a correction for T_1 signal decay during XY can be designed. Based on Eq. [2.4], magnetization spends, on average, 3/8 of every pulse duration along the z axis. The corrected echo times (TE_{corr}) are

$$\mathrm{TE}_{corr} = \mathrm{TE} - k * (\frac{3}{8} - \frac{3 * T_2}{8 * T_1}) * pw. \tag{2.7}$$

The resultant error is minimized over the physiologic range of T_1/T_2 and a reasonable range of pw/τ_{180} when $\delta \sim 0.066$. Since XY cycles the RF pulse throughout the xy plane (Table 2.1), this correction is less sensitive to resonance offset than MLEV or XY. Using this optimal value, T_2 error tends to be well within 1.5% for applications on a whole-body imager.

2.3.3 Experimental setup

Experiments were performed using the body coil of a 1.5 Tesla GE Signa. The role of the refocussing train was isolated using the following pulse sequence. A rectangular excitation pulse (90_x) is followed by a train of 180_y rectangular refocussing pulses or $90_x180_y90_x$ composite refocussing pulses applied in CPMG, MLEV, or XY. Lack of spoiling gradients during the train eliminates concerns about eddy currents. A final refocussing pulse is spoiled and slice-selective. Spatial-encoding is performed by rapid spiral acquisition after the slice-selective pulse. Subsequent excitation pulses are phase-cycled to remove any contribution from magnetization left along the z axis after the excitation pulse.

T_2 images were constructed using four echo times chosen to optimize SNR over the

physiological range of T_2 for MR oximetry (TE = 30, 78, 126, and 222 ms) [4, 21]. 30 ms of each echo time is required for slice selection and spatial encoding; the remainder is the duration of the refocussing train (0, 48, 96, and 192 ms). The number of refocussing pulses at each echo time is the duration of the refocussing train relative to the refocussing interval ((TE-30)/τ_{180}). To calculate T_2, signal decays within each voxel were fitted as a monoexponential decay using a weighted least-squares approach [35].

2.3.4 Experiment 1: T_1 decay during composite pulses

This experiment demonstrated the sensitivity of the T_2 measurement to T_1 signal decay during MLEV trains of well-tuned $90_x180_y90_x$ composite pulses and verified the performance of the TE correction. By varying the pulsewidth while holding τ_{180} constant on subsequent measurements (τ_{180} = 12 ms), the signal decay curves from a 0.097 mM $MnCl_2$ solution with independently measured relaxation times (T_2 = 160± 2ms, T_1 = 1120 ± 2ms) were acquired over a range of pw/τ_{180} from 0.04 to 0.32. Using these curves, T_2 values were calculated and compared with and without the correction scheme (δ = 0.088).

The independent T_2 measurement was performed using high RF amplitude ($\frac{\gamma}{2\pi}B_1$ = 1 kHz) rectangular pulses in a MLEV pattern. T_2 was within the standard deviation using refocussing intervals of both 6 and 24 ms. This insensitivity suggests ΔB_1 was not significant. The independent T_1 measurement was performed using an inversion recovery sequence on a 1.5 Tesla spectrometer (SMIS, Surrey).

2.3.5 Experiment 2: Absolute accuracy of the T_2 measurement

This experiment demonstrated the ability of MLEV patterns of well-tuned $90_x180_y90_x$ composite pulses (γB_1 = 620 Hz, pw/τ_{180} = 0.13) and the correction scheme (δ = 0.088) to preserve accurate T_2 contrast using a 1.5 Tesla spectrometer (SMIS, Surrey) as a gold stan-

dard. Measurements were made from $MnCl_2$ solutions over a range of relaxation times (T_2=50-350 ms) on both the imager and the spectrometer. To verify the insensitivity of the spectrometer-measured relaxation times to ΔB_0 and spin-locking, these measurements were performed with high RF amplitudes ($\frac{\gamma}{2\pi}B_1 \sim 33$ kHz) at two refocussing intervals ($\tau_{180} = 1$ and 6 ms).

2.3.6 Experiment 3: Reliability of the T_2 measurement

To verify the inadequacy of rectangular pulses for T_2 quantitation insensitive to ΔB_0 and ΔB_1 and to investigate the efficacy of the proposed refocussing trains, T_2 error was mapped to RF and static field inhomogeneities using CPMG, MLEV, and XY trains of both rectangular and composite pulses. Using both the experiment and the computer model, measurements were made at refocussing intervals of both 6 and 24 ms over static field offsets to ± 2 ppm and RF amplitudes from 0.7 to 1.4 times the ideal RF amplitude ($\frac{\gamma}{2\pi}B_{1,norm} = 620$ Hz). Simulated data were sampled at every pair of integer-valued offsets (ΔB_0, ΔB_1).

To facilitate rapid error mapping, an axial magnetic field gradient ($G_x \sim 12$ Hz/cm) was applied across a 20 cm diameter beaker containing $MnCl_2$ solution ($T_2 = 160$ ms, $T_1 = 1120$ ms) throughout the entire refocussing train. An axial T_2 image (2.5 mm x 2.5 mm x 1 cm resolution) obtained in the presence of this gradient illustrates the sensitivity of the T_2 measurement to a broad range of resonance offsets. By deliberate mistuning of the RF amplifier on separate measurements, the sensitivity of the T_2 measurement to errors in both RF and static field amplitude could be mapped efficiently.

2.4 Results and Discussion

2.4.1 Experiment 1: T_1 signal decay during composite pulses

Figure 2.7 verifies the severity of T_1 signal decay during composite pulses on the T_2 measurement. Both the experimentally measured and the simulated T_2 error increase relative to the independently measured relaxation time, as a proportionately longer period of time is spent along M_z during the refocussing train. Error is excessive when $pw/\tau_{180} > 0.1$. The standard deviation of repeated measurements of T_2 was about $\pm 1\%$.

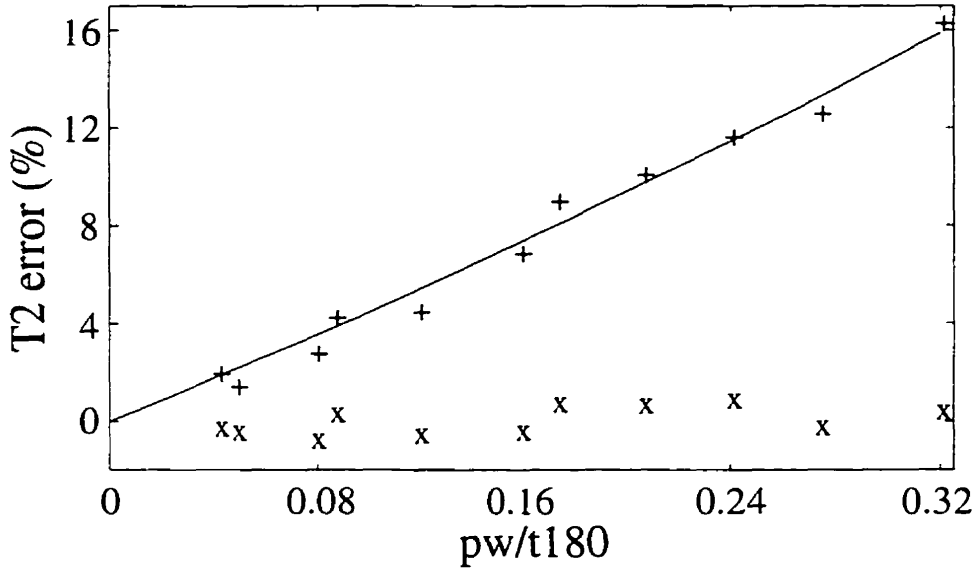

Figure 2.7: T_2 error following a train of $90_x180_y90_x$ composite pulses with (x) and without (+) the correction scheme. The solid line depicts the simulated T_2 error expected for a $MnCl_2$ solution with $T_1/T_2 = 1120/160$. Agreement between the experimental and the simulated T_2 errors is very good. T_2 accuracy clearly becomes degraded as the period spent along M_z during each pulse ($\propto pw$) increases relative to the period between pulses (τ_{180}). The correction must be implemented for T_2 accuracy within 5% when $pw/\tau_{180} \geq 0.1$.

We are interested in a range of pw/τ_{180} from about 0.05 to 0.32. The corresponding error in T_2 will range from 2 to 17% over the physiologic range of T_1/T_2. This will be a significant source of error in any T_2 measurement which uses composite refocussing pulses on a whole-body imager. Based on the results displayed in Fig. 2.7, this error can be

compensated during trains of simple $90_x180_y90_x$ composite pulses. Thus I have a correction scheme that is easy to implement on any system with knowledge of only user-defined sequence parameters (pw, τ_{180}).

2.4.2 Experiment 2: Absolute accuracy of the T_2 measurement

Spectrometer-measured T_2 values of water doped with $MnCl_2$ agreed within 0.5% for τ_{180} = 1 and 6 ms. The constancy of these values illustrates the insensitivity of the measured relaxation times to ΔB_0, ΔB_1, and spin-locking. Figure 2.8 demonstrates the absolute accuracy of the T_2 measurement technique. Imager-measured relaxation times underestimate the spectrometer-measured values slightly, yet all values agree within 5%.

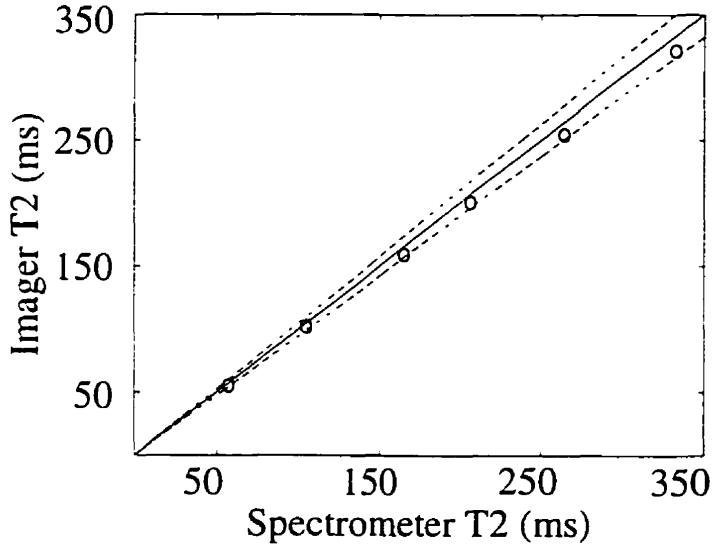

Figure 2.8: Comparison of imager-measured and spectrometer-measured T_2 relaxation times. The circles depict the corresponding relaxation times on the two systems. The solid line represents the identity line. The dashed lines represent correlation within ±5%. With the TE correction, the proposed refocussing train preserves accurate T_2 contrast, within 5% of the spectrometer-measured values, over a broad range of relaxation times.

2.4.3 Experiment 3: Reliability of the T_2 measurement

For simplicity, I display the maps of T_2 error as contour plots. Each point on these plots depicts the T_2 error which results within the refocussing train at a given $\Delta B_0/B_1$ and ΔB_1. However, within a practical measurement, a spatial distribution of ΔB_0 and ΔB_1 will exist within each image voxel. To ensure T_2 accuracy, T_2 error should be small mapped over the range of offsets present within each voxel of interest.

Figure 2.9 maps the dependence of T_2 error on RF and static field inhomogeneities using rectangular pulses. The inadequacy of rectangular pulses for *in-vivo* work is clearly illustrated. Error is excessive at small ΔB_1 when magnetization is orthogonal to the axis of rotation: when ϕ is approximately $n\pi/2$ where n is an odd integer. For $n = \pm 1$, such phase offsets occur in Fig. 2.9(a) for $\Delta B_0 = 0.33$ ppm and in Fig. 2.9(b) for $\Delta B_0 = 1.3$ ppm.

Figure 2.10 maps the sensitivity of T_2 error to RF and static field offsets using CPMG, MLEV, and XY trains of composite pulses with $\tau_{180} = 24$ and 6 ms. Composite pulses are essential to achieve high measurement accuracy. Selection of RF cycling pattern is less significant. With our TE correction, MLEV ($\delta = 0.088$) and XY ($\delta = 0.066$) trains of low RF amplitude composite pulses ($\frac{\gamma}{2\pi} B_{1,norm} = 620$ Hz) provide a useful operating region to about ± 1.5 ppm in ΔB_0 and $\pm$ 20% in ΔB_1 for $\tau_{180} = 24$ ms (Fig. 2.10(c and e)), and to about ± 1 ppm in ΔB_0 and $\pm 20\%$ in ΔB_1 for $\tau_{180} = 6$ ms (Fig. 2.10(d and f)). Using CPMG (Fig. 2.10(a and b)), the size of the useful region decreased slightly.

Although, MLEV and XY do not provide a significant qualitative improvement over CPMG under controlled conditions, I would argue the need for better RF cycling than CPMG within a general T_2 measurement. By consideration of the mechanics of error compensation through RF cycling patterns, I can show that MLEV and XY preserve both the M_{xy} component and the M_z component more robustly than does CPMG, thus making them preferable for *in-vivo* T_2 quantitation.

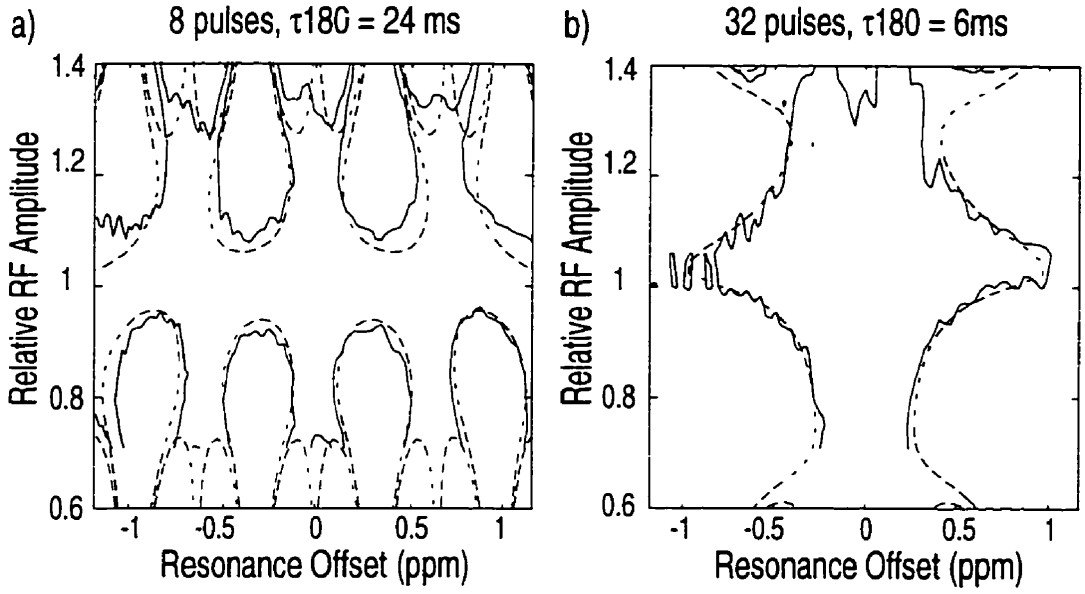

Figure 2.9: Mapping of T_2 measurement error to ΔB_0 and ΔB_1 during MLEV trains of rectangular pulses for (a) $\tau_{180} = 24$ ms and (b) $\tau_{180} = 6$ ms. Simulated and experimental measurements are shown using dashed and solid lines respectively. Each point on these plots indicates T_2 error following a refocussing train played in the presence of given ΔB_1 and ΔB_0 ($\frac{\gamma}{2\pi} B_{1,norm} = 620$ Hz). Contour lines depict ΔB_0 and ΔB_1 past which T_2 error is excessive ($> 5\%$). T_2 and T_1 were 160 and 1120 ms respectively.

RF cycling patterns are devised from sequences of RF pulses which recursively self-compensate for pulse errors. Each recursion is itself a self-compensating pattern of refocussing pulses. Longer recursions provide greater ΔB_0 and ΔB_1 insensitivity. However, with limits to ΔB_0 and ΔB_1 compensation following a given recursion, refocussing may be incomplete leading to signal loss.

CPMG uses a simple recursion kernel ($180_y - 180_y$) to correct for ΔB_1 following every second pulse. However, the simultaneous effects of ΔB_0 and ΔB_1 will not be corrected for fully. As the same two-pulse pattern is repeated continually through the refocussing train, any residual two-pulse error will accumulate and the measured signal will decrease.

Unlike CPMG, MLEV and XY do not constrain the recursive expansion. Instead, ΔB_0 and ΔB_1 insensitivity improves with successive recursions (every 2^{nth} pulse), essentially

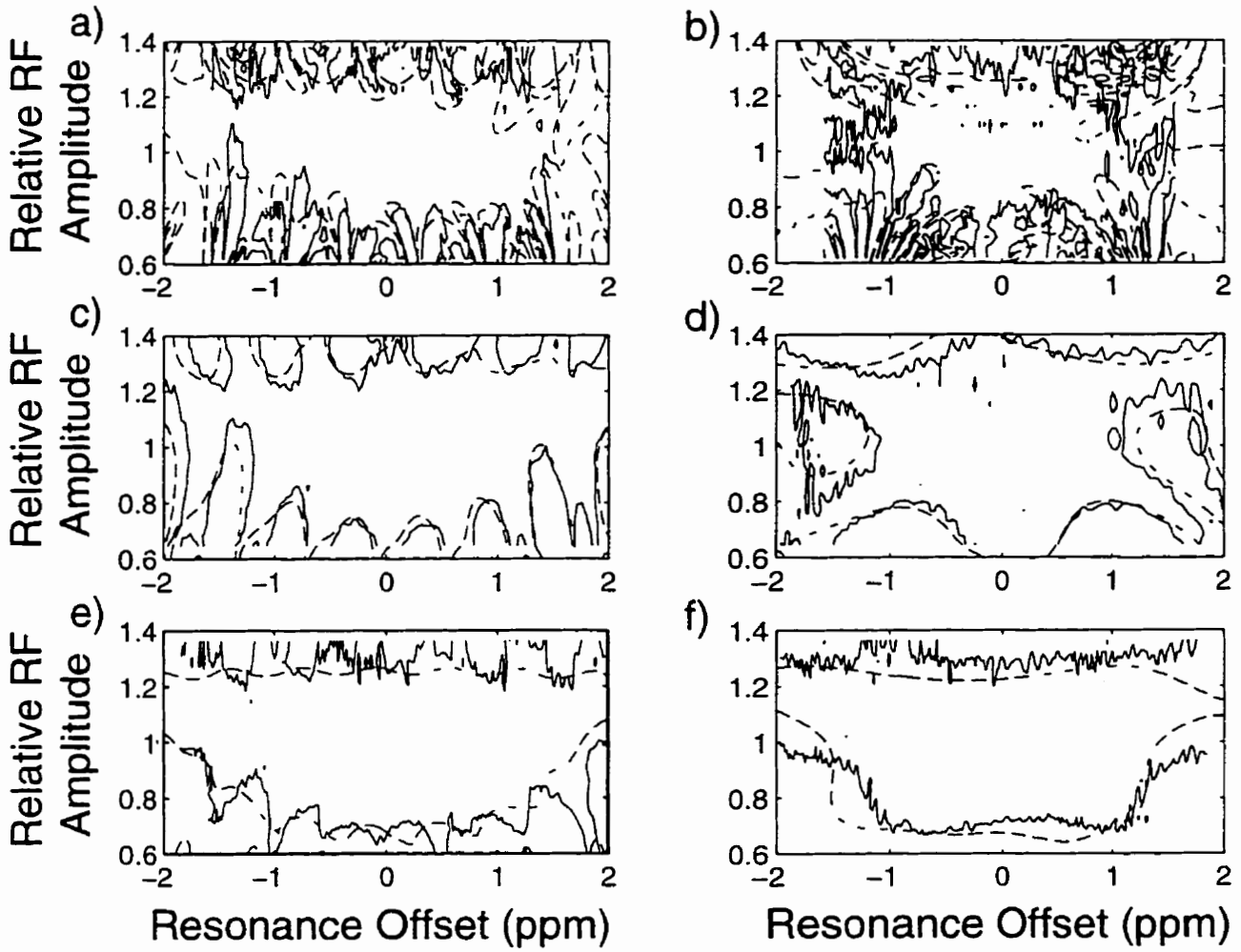

Figure 2.10: Mapping of T_2 measurement error to ΔB_0 and ΔB_1 using composite pulses; using CPMG with (a) $\tau_{180} = 24$ ms and (b) $\tau_{180} = 6$ ms; using MLEV with (c) $\tau_{180} = 24$ ms and (d) $\tau_{180} = 6$ ms; and using XY with (e) $\tau_{180} = 24$ ms and (f) $\tau_{180} = 6$ ms. The TE correction was implemented ($\delta \sim 0.088$ using CPMG and MLEV, 0.066 using XY). See Fig. 2.9. for details of relaxation times, and the ideal RF amplitude.

accounting for progressively higher-order error terms. Hence, MLEV and XY yield better refocussing than CPMG farther into the refocussing train.

At a given RF amplitude, MLEV and XY have several advantages over CPMG for T_2 quantitation:

1. More of the desired signal is refocussed with the proper phase within the xy plane at each data acquisition. Using simulated data, Fig. 2.11 maps the magnitude and phase of the M_{xy} component to RF and static field inhomogeneities following CPMG, MLEV, and XY trains of composite pulses ($\frac{\gamma}{2\pi}B_{1,norm} = 620$ Hz, $\tau_{180} = 12$ ms). Hence, long CPMG trains are more susceptible than MLEV or XY trains to signal loss on a whole-body imager due to longitudinal storage, or to intravoxel dephasing if there is a range of ΔB_0 or ΔB_1 across a voxel. This agrees with my experimental observation that T_2 mapping using CPMG was more sensitive than MLEV or XY to large ΔB_0 and ΔB_1. This may also explain the poorer agreement between experiment and simulation demonstrated using CPMG than with MLEV or XY (Fig. 2.10).

2. Less magnetization left along the z axis following a poor excitation will be rotated to the xy plane and measured. Using simulated data, Fig. 2.12 depicts the fraction of this component which contributes to the measured signal following a CPMG train of 16 low RF amplitude composite pulses ($\frac{\gamma}{2\pi}B_{1,norm} = 620$ Hz, $\tau_{180} = 12$ ms). This contribution gains added significance in long refocussing trains as the desired signal becomes attenuated by T_2 decay. Using 16-pulse MLEV or XY trains, this contribution tends to be well within 2% over typical ΔB_1 and ΔB_0. In my experiment, this component is removed by RF cycling the excitation; however, cancellation may be imperfect *in-vivo* due to motion between excitations.

As a consequence of improved refocussing, both MLEV and XY tend to overestimate T_2 excessively at larger pulse errors. At these large errors, significant magnetization may

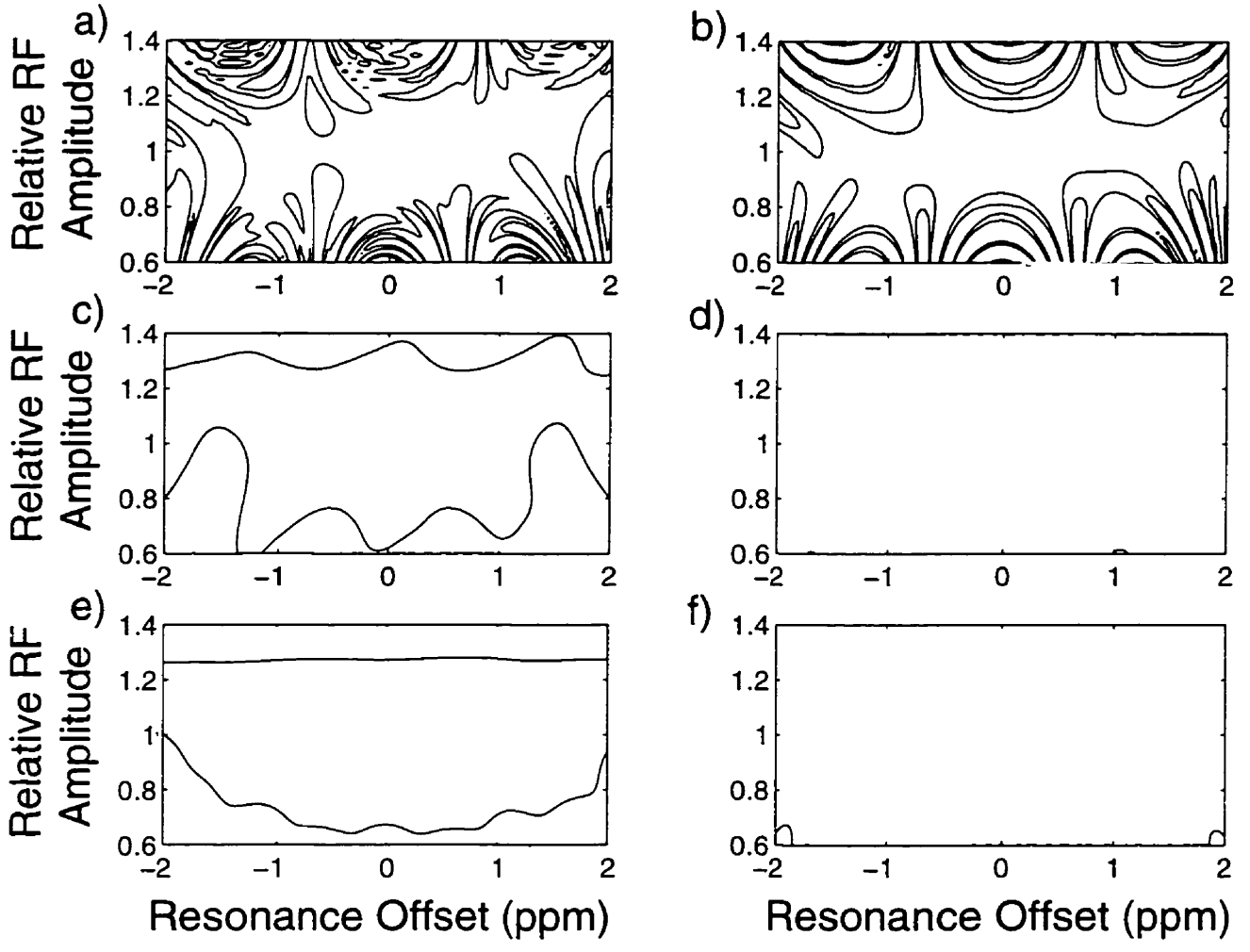

Figure 2.11: Simulated refocussing performance of 16 composite pulses in the presence of RF and static field inhomogeneities: (a) normalized magnitude and (b) phase using CPMG; (c) normalized magnitude and (d) phase using MLEV; and (e) normalized magnitude and (f) phase using XY. The first contour lines represent 5% error in magnitude and 10° error in phase respectively. Contour lines on the phase plots increment by 20°. See Fig. 2.9 for details of relaxation times, and the ideal RF amplitude.

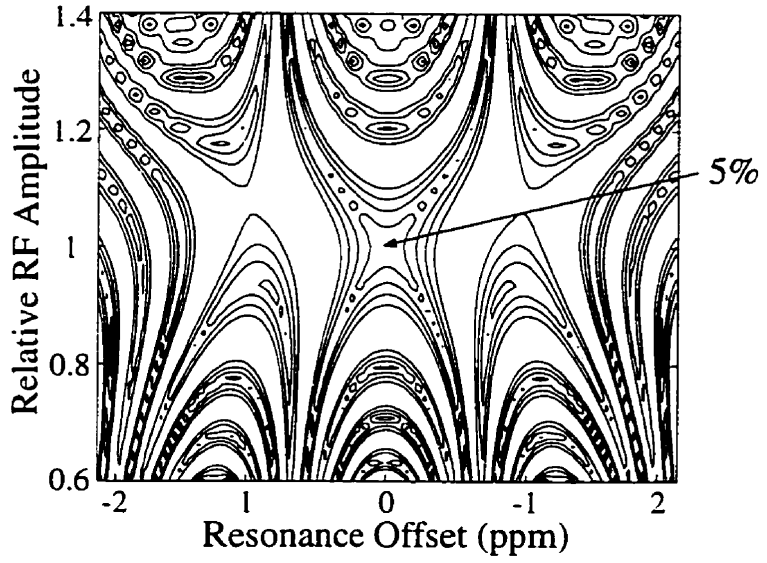

Figure 2.12: Fraction of the longitudinal magnetization rotated to the transverse plane following a CPMG train of 16 composite pulses in the presence of RF and static field inhomogeneities. Contour lines start at 5% and increment by 10%. See Fig. 2.9 for details of relaxation times and sequence parameters. Using MLEV and XY, the corresponding contributions were within 3% across the entire plane and are not shown.

be stored along the z axis at intermediate stages of the cycling pattern when refocussing is poorer (not after 2^n pulses). This magnetization will be preferentially returned to the xy plane at later data acquisitions when refocussing is improved. As a result, both the measured signal and the T_2 measurement tend to be overestimated outside the useful operating region (Fig 2.10 (c-f) and Fig 2.11 (c and e)).

Of interest are the regions of T_2 error which appear at frequency offsets $\sim \pm 1.2$ ppm in Fig. 2.10(d). In these regions, T_2 is underestimated. Recall that off-resonance magnetization is less sensitive to T_1 signal decay during composite pulses (Fig. 2.5). Overcompensation by the TE correction was predicted to be excessive for magnetization along the x axis when $pw/\tau_{180} > 0.2$. In Fig. 2.10(d), $\phi = \pi/2$ for $\Delta B_0 \sim 1.3$ ppm, and $pw/\tau_{180} = 0.27$; hence, these regions are an artifact of the TE correction. Using CPMG (Fig. 2.10(b)), this error is masked due to increased signal loss at large pulse errors. The TE correction for XY is less sensitive to resonance offset and this region is not observed in Fig. 2.10(f).

Using these refocussing trains, the achievement of larger operating regions than those illustrated in Fig. 2.10 requires higher RF amplitudes. Such an increase has two effects: 1) $\Delta B_0/B_1$ is decreased; and 2) pw/τ_{180} is decreased. Simulations suggest that, with my correction, MLEV and XY trains of high RF amplitude pulses ($\frac{\gamma}{2\pi}B_{1,norm}$ = 1 kHz) provide T_2 accuracy within 5% over ΔB_1 and ΔB_0 to approximately ±20% and ±2 ppm (Fig. 2.13). CPMG is slightly less robust.

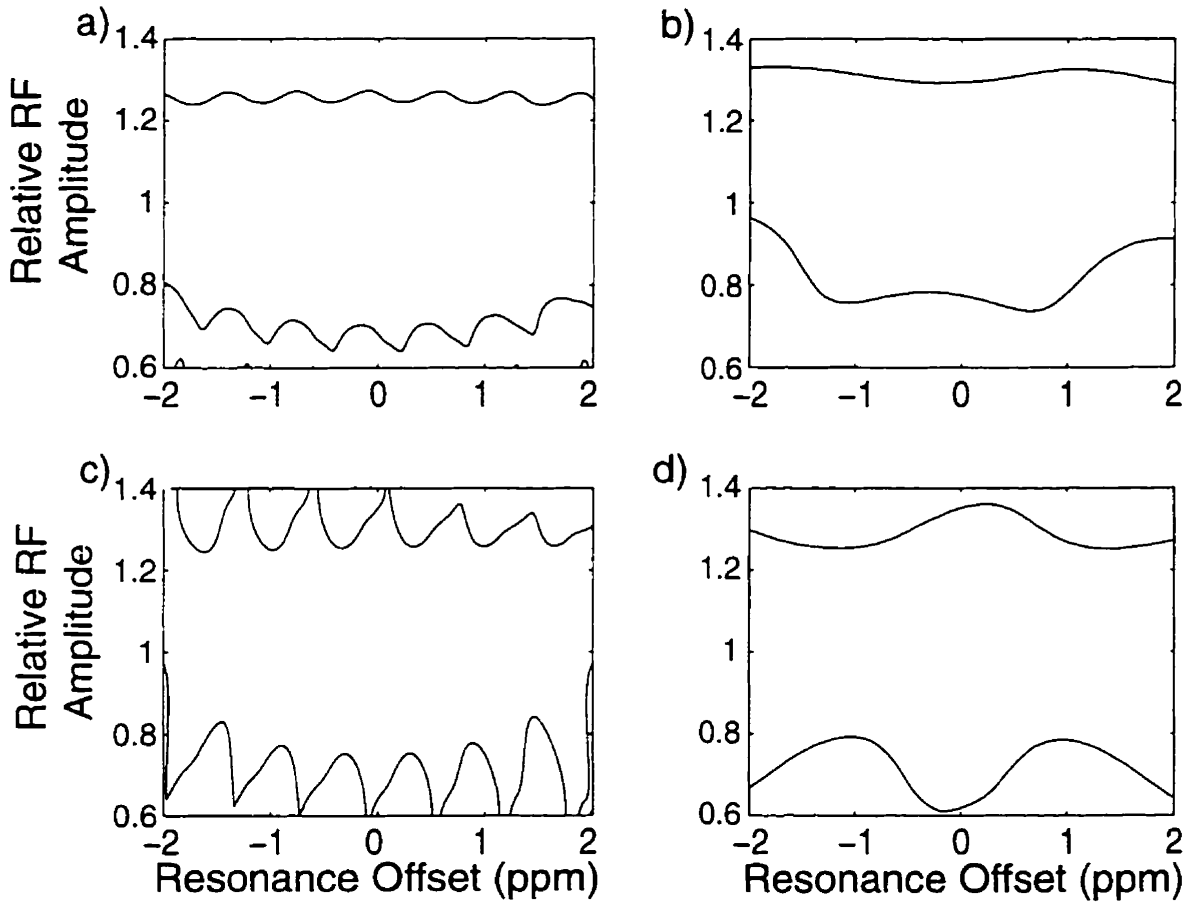

Figure 2.13: Mapping of simulated T_2 measurement error to RF and static field inhomogeneities using high RF amplitude composite pulses ($\frac{\gamma}{2\pi}B_1$ = 1 kHz): (a) MLEV, τ_{180} = 24 ms; (b) MLEV, τ_{180} = 6 ms; (c) XY, τ_{180} = 24 ms; and (d) XY, τ_{180} = 6 ms. Contour lines represent 5% error in T_2.

2.4.4 Practical issues

Trains of simple composite pulses and good RF-cycling patterns have several practical advantages over existing techniques:

1. Spoiler gradients are not implemented within the refocussing train. This is useful for avoiding RF phase shifts due to eddy currents, minimizing signal loss following non-ideal refocussing pulses and minimizing flow-dephasing for application to MR oximetry.

2. Simple $90_x180_y90_x$ composite pulses are used. In contrast to more complex refocussing pulses, these pulses have a) reduced heat deposition and b) a simple geometry which allows a straightforward correction for bias from T_1 signal decay during each pulse.

3. Short pulse durations ($pw \leq 1.6$ ms) at typical RF amplitudes allow for rapid refocussing, with minimum τ_{180} between 5 and 10 ms. This has application for the measurement of short relaxation times and for the prevention of signal loss due to flow through ΔB_0 [53].

These trains can be implemented in various configurations. I have demonstrated one in the current set of experiments - a train followed by a slice-selective refocussing pulse and an imaging acquisition. With this sequence, T_2 images can be constructed efficiently (80 seconds/TE with 2.5 mm by 2.5 mm resolution) despite long TR and phase-cycling of the excitation pulse. A more flexible variation includes the train in a magnetization preparation sequence [54, 55]. In this configuration, following contrast preparation, one can do multislice acquisitions by imaging different slices on different tip-downs or one can do faster 2D and 3D acquisitions by scanning different parts of k-space within a series of small tip-angle excitations. Another realization is to use a volumetric measurement and read out at various stages within the refocussing train [56]. This would reduce scan time and would allow for the evaluation of complicated signal decay behaviour in tissue. However, this approach is

unsuitable if flow is an issue. In addition, steps must be taken to minimize the effects of eddy currents during the read gradient [41]. For further improvement to the above configurations, a more robust refocussing pulse than the $90_x180_y90_x$ pulse can be implemented [48] with the appropriate TE correction. The increased insensitivity to ΔB_0 and ΔB_1 provided by these pulses will be useful within regions where the $90_x180_y90_x$ pulse is inadequate.

Chapter 3

Summary and Future Work

3.1 Summary

MR oximetry requires T_2 accuracy within 5% for oxygen saturation measurements to be clinically acceptable. To achieve this accuracy *in vivo*, the effects of imperfect refocussing pulses on the T_2 measurement must be taken into account. Current measurement techniques use good RF cycling patterns or good composite pulses to prevent signal loss. However, these techniques store magnetization temporarily along the z axis, either between rectangular pulses or during composite pulses, where magnetization decays more slowly with a time constant T_1. This dissertation focussed on the design and evaluation of a refocussing train capable of T_2 accuracy within 5% over conditions typical of a whole-body imager.

The resultant train design is both straightforward and effective. Simple composite pulses restrict T_1 decay between refocussing pulses. A practical correction scheme can compensate for T_1 decay during each composite pulse. Good RF cycling patterns prevent signal loss at each data acquisition. Using this combination, accuracy was demonstrated over a diverse range of conditions typical of the *in vivo* measurement. Comparative studies between imager-based and spectrometer-based T_2 measurements demonstrated excellent agreement.

3.2 Future Work

The overall goal of this project is to develop an *in vivo* T_2 measurement technique. For MR oximetry, this technique must be insensitive to the effects of vascular flow and bulk physiological motions within the chest cavity, as well as the constraints of a whole-body imager. The successful design and evaluation of the refocussing train for accuracy on a whole-body imager completes the first step in this development.

While future development of the T_2 measurement technique will continue to be guided by the oximetry application, it has broader application to MR tissue signal characterization in general. In this section I briefly outline the following: several possible directions for further work and their significance; the additional challenges which constrain each new development; and methods I will explore to overcome such challenges. The plan of study for the characterization of the signal decay from flowing blood is described in greater detail and some preliminary results are presented as a feasibility check.

Characterization of static tissue signal

Unlike previous studies which were less reliable due to poor measurement techniques, the current method should be effective within static regions *in vivo*. This will facilitate tissue characterization in static or slowly-moving regions such as the vertebral disks [57]. As well, any measurement technique using composite pulses can benefit from the correction scheme.

Moreover, characterization of the complicated signal decay behaviour exhibited within many tissues will require modifications to the data acquisition method. In general, the signal decay from tissues other than vascular blood must be fitted using multiple T_2 relaxation components. A multiexponential analysis requires frequent sampling of the signal decay. Using the current method, the signal at only a single echo time is sampled per excitation and the repetition time between excitations is long; hence, imaging times can become prohibitively

long when frequent sampling is required.

To address these time constraints, the design of multiple spin-echo techniques which allow for multiexponential analysis with shorter acquisition times on a whole-body imager is currently being explored [56]. Issues to consider include the effects of eddy currents associated with the readout gradient and whether CPMG, MLEV, XY, or spoiling, in conjunction with composite pulses, is most appropriate for adequate sampling of complicated signal decay behaviour.

Characterization of dynamic tissue signal

The more specific method using RF cycling patterns instead of spoiling gradients while avoiding spatially selective refocussing pulses may prove useful in dynamic regions in and around the heart and abdomen. In addition to facilitating oximetry studies within the great vessels and the characterization of moving tissue signal, a motion-insensitive refocussing train could enable a non-invasive evaluation of heart tissue viability following an infarction.

However, bulk cardiac and respiratory motions during the scan pose significant challenges to T_2 accuracy. Gating to the heart cycle 'freezes' cardiac motion, yet, variations in the R-R interval can lead to variable T_1 recovery between excitations and hence T_2 bias. As well, gating does not account for respiratory motion which can introduce image blur and hence overlap of signal from different regions.

To reduce the effects of bulk motion on T_2 accuracy, I will explore various motion-insensitive methods. These include improved methods for cardiac gating, improved methods for signal averaging, methods for respiratory motion compensation, and faster imaging techniques. One area of particular interest is the development of sequences which will permit measurements of T_2 within a breath-holding interval (20-30 seconds).

Characterization of flowing blood signal

For vascular studies, there is the additional challenge of making measurements in the presence of flow. Using the data acquisition methods described herein, the required accuracy (T_2 error within 5%) has been demonstrated within the superior mesenteric vein of a dog, where flows are slow [58]. To extend this work to measures in and around the heart, we require a T_2 measurement insensitive to the effects of significantly higher flows.

Of interest are the effects of flow through spatially-varying static and RF field inhomogeneities on the data acquisition method. In particular, phase accrual due to flow through ΔB_0 variations is compensated for following every even-numbered refocussing pulse when ΔB_0 can be modelled as a linear gradient [53]. This approximation should improve with faster refocussing as magnetization travels a shorter distance between each pulse pair.

To facilitate vascular T_2 measurements, we have designed the data acquisition for insensitivity to flow. T_2-weighted images are obtained using a MLEV pattern of $90_x180_y90_x$ composite refocussing pulses implemented into a flow insensitive magnetization preparation sequence (T_2 Prep) [59]. My echo time correction accounts for the effects of T_1 decay during each composite pulse [1]. RF cycling preserves T_2 contrast during the period between the end of the preparation and readout [55]. T_2's are calculated as a weighted least squares fit to signals measured at 4 echo times (1, 49, 97, 193 ms).

Flow insensitivity using this sequence is currently being evaluated in three steps. A computer model has been developed to explore the effects of flow through ΔB_0 and ΔB_1. The model is being verified through comparisons with T_2 measurements in a flow phantom. Measurements are being performed *in vivo* to verify that, with proper sequence design, flow effects on T_2 do not alter T_2 measurements within the femoral artery of human subjects. I elaborate on each step briefly in the following sections.

1. Computer model

The simulation described in Ch.2 has been modified to account for flow through spatially-varying RF and static field variations. Using experimentally-measured flow profiles, ΔB_0 maps, and ΔB_1 maps as input, the MR signal is simulated in the presence of flow.

2. Physical model

The flow phantom uses a peristaltic pump to drive fluid through a tube aligned along the bore of the magnet. A settling chamber removes any pulsatility. By systematically varying the flow rate, the field inhomogeneities, and the sequence parameters, the effects of spatially-varying ΔB_0 and ΔB_1 are isolated.

Comparisons of T_2 error within parallel studies using $MnCl_2$-doped water and cow blood ($\%O_2 > 95\%$) determine if the physical characteristics of blood (high viscosity, cell suspension) significantly alter the results. Preliminary measurements suggest such effects are not significant.

To verify the simulation, initial measurements will explore the effects of flow through ΔB_0 and ΔB_1 typical of the imaging situation in the leg on T_2 accuracy. Some of these results are presented in the feasiblity study which follows. Subsequent measurements will focus on the effects on T_2 accuracy of varying sequence parameters and introducing larger spatial variations of ΔB_0 and ΔB_1, with an eye to improving the data acquisition method.

3. Flow effects on vascular T_2 measurements

Based on the *in vitro* evaluation of flow effects on T_2, I should be able to demonstrate that, with proper parameter selection, T_2 error due to flow will not be significant over a wide range of flow conditions, including those associated with the femoral artery. To validate this statement, femoral artery T_2's are being compared with and without flow

restricted.

These studies require the inflation of a pressure cuff proximal to the imaging slice. Inflation to a pressure 10 mmHg higher than that for which a peripheral pulse could no longer be detected is sufficient to restrict flow. Compression is never for longer than 6 minutes. To reduce any effects on T_2 from red blood cell settling or arterial dilation, inflation is begun within a minute of data acquisition. To isolate the effects of flow, T_2 values obtained with and without the cuff inflated are being compared. To ensure adequate SNR, all measurements use the GP-flex receiver coil.

Feasibility study

To verify the simulation and examine the role of τ_{180}, a feasibility study explored the effects of flow on T_2 *in vitro*. T_2's were measured in $MnCl_2$-doped water (T_2 = 153±1 ms) over a broad range of flow rates and sequence parameters. ΔB_0 and ΔB_1 variations were typical of the imaging situation in the leg. At ±10 cm along the tube, approximately the maximum distance of flow at the latest echo time (TE = 193 ms), ΔB_1 was -10% and ΔB_0 was -1 ppm. Within this range, ΔB_0 varied in a quadratic fashion. TR was 2 seconds.

Agreement between the *in vitro* experiment and simulation is reasonable (Figure 3.1). Signal wash-in and inaccuracies in field mapping farther from the imaging slice may account for the differences seen. Measurements were insensitive to peak velocities less than 50 cm/s, especially with short τ_{180}. At higher flows and longer τ_{180}, the measurements tend to underestimate T_2. Improvements with faster refocussing indicates the primary source of signal loss is ΔB_0. The standard error in repeat measurements was about 1%.

The constancy of these values is highly suggestive that vascular signal characterization is a feasible goal. These results prompt a more rigorous consideration of the effects of flow on vascular T_2 accuracy.

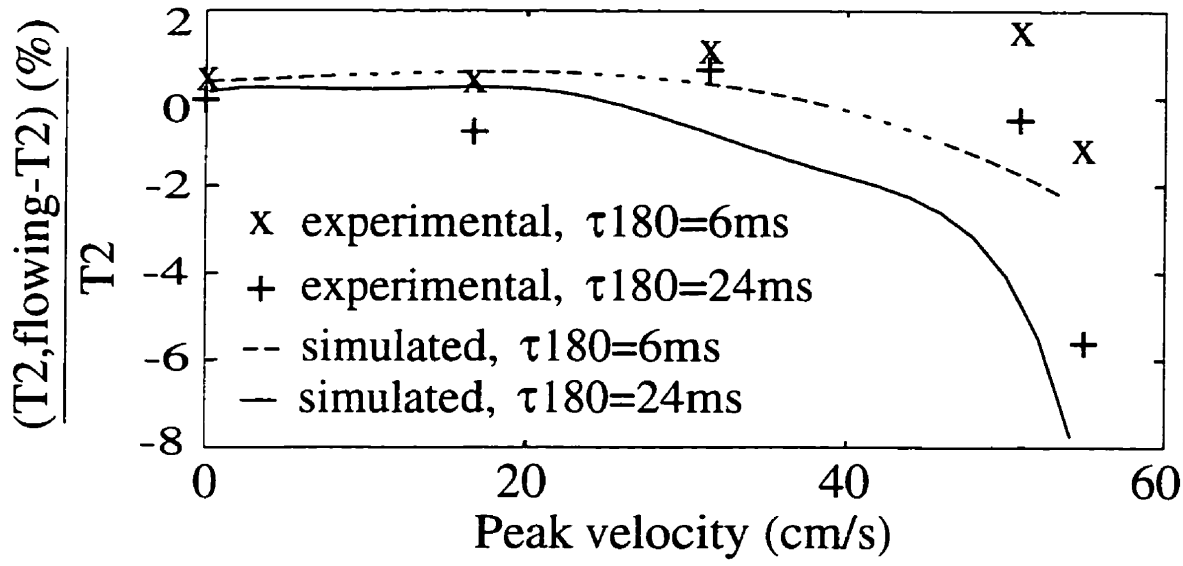

Figure 3.1: The sensitivity of T_2 to flow velocity at two refocussing intervals. At each refocussing interval, all experimentally-measured T_2 measurements agreed within 5%. A slight decrease in T_2 was observed at higher velocities. Results suggest this decrease to be excessive for peak flows > 50 cm/s and τ_{180} > 24 ms. The simulations assumed an actual T_2 value of 153.5 ms.

3.3 Conclusions

This work addresses the significant technical challenges which have limited the application of T_2 as a quantitative tool. Relatively simple composite pulses are essential for T_2 accuracy over constraints typical of a whole-body scanner. Bias from finite pulse durations must be corrected to yield accuracy within 5% when $pw/t_{180} > 0.1$. A simple yet robust correction scheme can be implemented with knowledge of sequence parameters only. RF cycling patterns better than CPMG provide only a minor improvement in shorter refocussing trains. It may be prudent to implement MLEV or XY in longer refocussing trains.

Good T_2 accuracy within static volumes and promising results in the presence of flow suggests the feasibility of MR oximetry for the assessment of shunts in congenital heart disease. Further work is required to optimize the measurement technique for insensitivity to the additional demands of the *in vivo* environment including motion ands higher flows.

Bibliography

[1] H. Larsson, J. Frederiksen, L. Kjaer, O. Henriksen, J. Olesen, In vivo determination of T_1 and T_2 in the brain of patients with severe but stable multiple sclerosis, *Magnetic Resonance in Medicine* **7**, 43–55 (1988).

[2] V. Rajanayagam, M. Fabry, J. Gore, In vivo quantitation of water content in muscle tissues by NMR imaging, *Magnetic Resonance Imaging* **9**, 621–625 (1991).

[3] K. Thulborn, J. Waterton, P. Matthews, G. Radda, Oxygenation dependence of the transverse relaxation time of water protons in whole blood at high field, *Biochimica et Biophysica Acta* **714**, 265–270 (1982).

[4] G. Wright, B. Hu, A. Macovski, Estimating oxygen saturation of blood in vivo with MRI at 1.5 T, *Journal of Magnetic Resonance Imaging* , 275–283 (1991).

[5] G. B. Klintmalm, R. Cronestrand, A. Wennmalm, *et al.*, Human renal allograft blood flow, oxygen extraction, and prostaglandin release: Their bearing on graft function, *Surgery* **95**, 427–32 (1984).

[6] E. Braunwald, "Heart Disease: A Textbook of Cardiovascular Medicine", Saunders, 1989.

[7] W. Hundley, H. Li, R. Lange, D. Pfeifer, B. Meshack, J. Willard, C. Landau, D. Willet, L. Hillis, R. Peshock, Assessment of left-to-right shunting by velocity-encoded, phase difference magnetic resonance imaging, *Circulation* **91**, 2955–2960 (1995).

[8] R. Gill, Measurement of blood flow by ultrasound: Accuracy and sources of error, *Ultrasound in Medicine and Biology* **11**, 625–641 (1985).

[9] W. Grossman, "Cardiac Catheterization and Angiography", chapter Shunt Detection and Measurement, pp. 155–168, Lea and Febiger, Philadelphia, 3 edition, 1986.

[10] D. Benaron, W. Benitz, R. Ariagno, D. Stevenson, Noninvasive methods for estimating in vivo oxygenation, *Clinical Pediatrics* . 258–273 (1992).

[11] M. D. Freed, O. S. Miettinen, A. S. Nadas, Oximetric detection of intracardiac left-to-right shunts, *British Heart Journal* **42**, 690–694 (1979).

[12] S. C. Cassidy, K. G. Schmidt, G. F. van Hare, P. S. Stanger, D. F. Teitel, Complications of pediatric cardiac catheterization: A three-year study, *Journal of the American College of Cardiology* **19**, 1285–1293 (1992).

[13] D. Mancini, L. Bolinger, H. Li, K. Kendrick, B. Chance, J. Wilson, Validation of near-infrared spectroscopy in humans, *Journal of Applied Physiology* **77**, 2740–2747 (1994).

[14] D. Eidelberg, G. Johnson, D. Barnes, *et al.*, Fluorine-19 NMR imaging of blood oxygenation in the brain, *Magnetic Resonance in Medicine* **6**, 344–52 (1988).

[15] C. Sotak, P. Hees, H. Huang, M. Hung, C. Krespan, S. Raynolds, A new perfluorocarbon for use in Fluorine-19 magnetic resonance imaging and spectroscopy, *Magnetic Resonance in Medicine* **29**, 188–195 (1993).

[16] T. Jue, S. Anderson, ^{1}H NMR observation of tissue myoglobin: an indicator of cellular oxygenation in vivo, *Magnetic Resonance in Medicine* **13**, 524–8 (1990).

[17] F. Goda, K. Liu, T. Walczak, J. O'Hara, J. Jiang, H. Swartz, In vivo oximetry using EPR and India ink, *Magnetic Resonance in Medicine* **33**, 237–245 (1995).

[18] D. Chien, D. Levin, C. Anderson, MR gradient echo imaging of intravscular blood oxygenation: T2* determination in the presence of flow, *in* "Second SMR", volume 2, p. 773, 1994.

[19] S. Lai, E. Haacke, W. Lin, D. Chien, D.Levin, In vivo measurement of cerebral venous blood oxygenation with MRI, *in* "Third SMR", volume 2, p. 849, 1995.

[20] G.Wright, P. Nguyen, Calibration issues for MR oximetry, *in* "Third SMR", volume 2, p. 1052, 1995.

[21] G. Wright, K. Li, B. Hu, L. Pelc, H. Wegmueller, R. Dalman, J. Brittain, A. Macovski, Error analysis for MR oximetry in vivo, *Twelfth Annual Meeting of Society of Magnetic Resonance in Medicine* , 141 (1993).

[22] E. Hahn, Spin echoes, *Physical Review* **80**, 580–594 (1950).

[23] A. MacKay, K. Whittall, J. Adler, D. Li, D. Paty, D. Graeb, In vivo visualization of myelin water in brain by magnetic resonance, *Magnetic Resonance in Medicine* **31**, 673–677 (1994).

[24] C. Jones, B. Rutt, Quantitative accurate T_2 comparison between multi-echo 3D FSE and CSE MRI, volume 3, p. 1065, Nice, France, 1995, Proc. 3rd Scientific Meeting of the Society of Magnetic Resonance.

[25] R. Vold, R. Vold, H. Simon, Errors in measurements of transverse relaxation rates, *Journal of Magnetic Resonance* **11**, 283–298 (1973).

[26] D. Hughes, Errors in T_2 values measured with the Carr-Purcell-Meiboom-Gill pulsed NMR sequence, *Journal of Magnetic Resonance* **26**, 481–489 (1977).

[27] S. Majumdar, S. Orphanoudakis, A. Gmitro, M. O'Donnell, J. Gore, Errors in the measurements of T2 using multiple-echo MRI techniques: I. effects of radiofrequency pulse imperfections, *Magnetic Resonance in Medicine* **3**, 397–417 (1986).

[28] S. Majumdar, S. Orphanoudakis, A. Gmitro, M. O'Donnell, J. Gore, Errors in the measurements of T2 using multiple-echo MRI techniques: II. effects of static field inhomogeneity, *Magnetic Resonance in Medicine* **3**, 562–574 (1986).

[29] D. Woessner, Effect of diffusion in nuclear magnetic resonance spin echo experiments, *Journal of Chemical Physics* **34**, 2057–2061 (1961).

[30] J. Schenck, The role of magnetic susceptibility in magnetic resonance imaging: MRI magnetic compatibility of the first and second kinds, *Medical Physics* **23**, 815–850 (1996).

[31] C. Poon, "Relaxation Time Measurement and Fat/Water Quantification using Magnetic Resonance Imaging: Technical Developments and Clinical Applications", PhD thesis, University of Toronto, Toronto, Ont. Canada, 1992.

[32] P. Bottomley, T. Foster, R. Argersinger, L. Pfeifer, A review of normal tissue hydrogen NMR relaxation times and relaxation mechanisms from 1-100 MHz: Dependence on tissue type, NMR frequency, temperature, species, excision, and age, *Medical Physics* **11**, 425–448 (July/August 1984).

[33] P. A. Bottomley, C. J. Hardy, R. E. Argersinger, G. Allen-Moore, A review of ^1H nuclear magnetic resonance relaxation in pathology: Are T_1 and T_2 diagnostic?, *Medical Physics* **14**, 1–37 (1987).

[34] C. Poon, R. Henkelman, Practical T2 quantitation for clinical applications, *Journal of Magnetic Resonance Imaging* **2**, 541–553 (1992).

[35] J. MacFall, S. Riederer, H. Wang, An analysis of noise propagation in computed T_2, pseudodensity, and synthetic spin-echo images, *Medical Physics* **13**, 282–292 (1986).

[36] R. Graumann, A. Oppelt, E. Stetter, Multiple-spin-echo imaging with a 2D Fourier method, *Magnetic Resonance in Medicine* **3**, 707–721 (1986).

[37] A. Crawley, R. Henkelman, Errors in T_2 estimation using multislice multiple-echo imaging, *Magnetic Resonance in Medicine* **4**, 34–47 (1987).

[38] R. Breger, F. Werhli, H. Charles, J. MacFall, V. Haughton, Reproducibility of relaxation and spin-density parameters in phantoms and the human brain measured by MR imaging at 1.5 T, *Magnetic Resonance in Medicine* **3**, 649–662 (1986).

[39] J. MacFall, F. Wehrli, R. Breger, G. Johnson, Methodology for the measurement and analysis of relaxation times in proton imaging, *Magnetic Resonance Imaging* **5**, 209–220 (1987).

[40] M. Masterson, R. McGary, Accuracy and reproducibility of image derived relaxation times on a clinical 1.5 T magnetic resonance scanner, *Medical Physics* **16**, 225–233 (1989).

[41] R. Hinks, K. Kohli, S. Washburn, Fast spin-echo prescan for artifact reduction, volume 2, p. 634, Nice, France, 1995, Proc. 3rd Scientific Meeting of the Society of Magnetic Resonance.

[42] S. Meiboom, D. Gill, Modified spin-echo method for measuring nuclear relaxation times, *Review of Scientific Instruments* **29**, 688–691 (1958).

[43] M. Levitt, R. Freeman, T. Frenkiel, Broadband decoupling in high-resolution nuclear magnetic resonance spectroscopy, *Advances in Magnetic Resonance* **11**, 47 (1983).

[44] A. Shaka, S. Rucker, A. Pines, Iterative Carr-Purcell trains, *Journal of Magnetic Resonance* **77**, 606–611 (1988).

[45] A. Maudsley, Modified Carr-Purcell-Meiboom-Gill sequence for NMR fourier imaging applications, *Journal of Magnetic Resonance* **69**, 488–491 (1986).

[46] T. Gullion, New, compensated Carr-Purcell sequences, *Journal of Magnetic Resonance* **89**, 479–484 (1990).

[47] T. Gullion, The effect of amplitude imbalance on compensated Carr-Purcell sequences, *Journal of Magnetic Resonance* **101**, 320–323 (1993).

[48] M. Levitt, Composite pulses, *Progress in NMR Spectroscopy* **18**, 61–122 (1986).

[49] M. Levitt, R. Freeman, Compensation for pulse imperfections in NMR spin echo experiments, *Journal of Magnetic Resonance* **43**, 65–80 (1981).

[50] C. Poon, R. Henkelman, 180^o refocusing pulses which are insensitive to static and radiofrequency field inhomogeneity, *Journal of Magnetic Resonance* **99**, 45–55 (1992).

[51] R. Mulkern, M. Williams, The general solution to the Bloch equation with constant RF and relaxation terms: application to saturation and slice selection, *Medical Physics* **20**, 5–13 (1993).

[52] G. E. Santyr, R. M. Henkelman, M. J. Bronskill, Variation in measured transverse relaxation in tissue resulting from spin locking with the CPMG sequence, *Journal of Magnetic Resonance* **79**, 28–44 (1988).

[53] D. G. Nishimura, A. Macovski, J. M. Pauly, Magnetic resonance angiography, *IEEE Transactions on Medical Imaging* **MI-5**, 140–151 (1986).

[54] J. Brittain, B. Hu, G. Wright, C. Meyer, A. Macovski, D. Nishimura, Coronary angiography with magnetization-prepared T_2 contrast, *Magnetic Resonance in Medicine* **33**, 689–696 (1995).

[55] G. Wright, J. Brittain, J. Stainsby, Preserving T_1 or T_2 contrast in magnetization preparation sequences, volume 3, p. 1474, New York, USA, 1996, Proc. 4th Scientific Meeting of the Society of Magnetic Resonance.

[56] J. Stainsby, J. Yu, W. Foltz, G. Wright, Monitoring blood oxygenation in a microcirculation model, volume 2, p. 1312, New York, USA, 1996, Proc. 4th Scientific Meeting of the Society of Magnetic Resonance.

[57] K. Fechner, G. Gold, G. Wright, I. Mitsui, J. Pauly, A. Hargens, Accurate long and short T_2 species measurement in intervertebral discs *in vivo*, Submitted to 5th Scientific Meeting of the Society of Magnetic Resonance, 1997.

[58] K. Li, G. Wright, L. Pelc, R. Dalman, J. Brittain, H. Wegmueller, D. Lin, C. Song, Oxygen saturation of blood in the superior mesenteric vein: In vivo verification of MR imaging measurements in a canine model, *Radiology* **194**, 321–326 (1995).

[59] J. Brittain, G. Wright, J. Pauly, A. Macovski, Flow-insensitive magnetization-prepared T2 measurement, *Twelfth Annual Meeting of Society of Magn. Reson. Med.* , 1216 (1993).

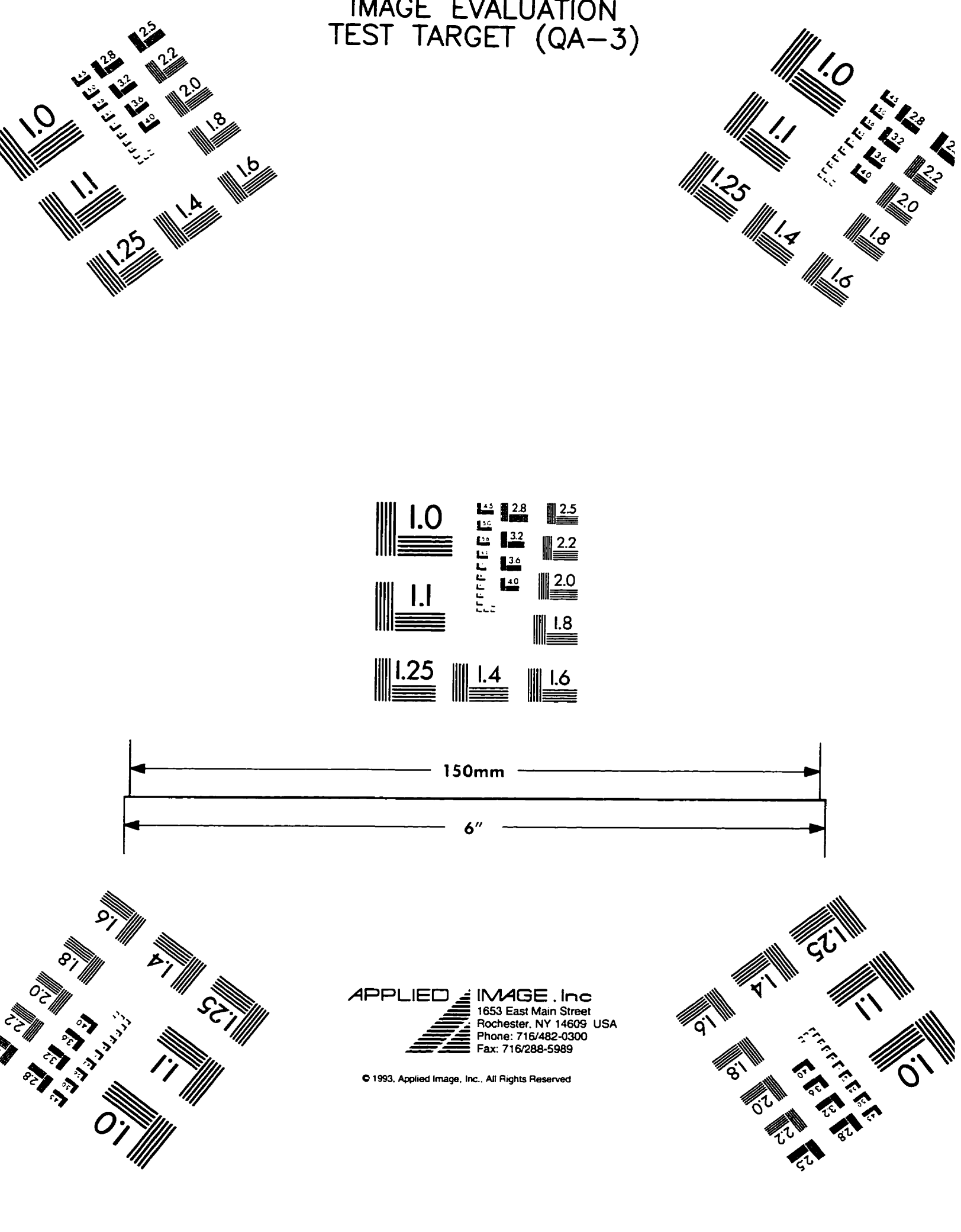

APPLIED IMAGE, Inc
1653 East Main Street
Rochester, NY 14609 USA
Phone: 716/482-0300
Fax: 716/288-5989